

Chaotic dynamics of the Hénon map and neuronal input–output: A comparison with neurophysiological data

Cite as: Chaos 33, 043111 (2023); <https://doi.org/10.1063/5.0142773>

Submitted: 17 January 2023 • Accepted: 10 March 2023 • Published Online: 03 April 2023

 Natalí Guisande,  Monserrat Pallares di Nunzio,  Nataniel Martinez, et al.



View Online



Export Citation



CrossMark



Chaos

Special Topic: Nonlinear Model
Reduction From Equations and Data

Submit Today!

Chaotic dynamics of the Hénon map and neuronal input-output: A comparison with neurophysiological data

Cite as: Chaos 33, 043111 (2023); doi: 10.1063/5.0142773

Submitted: 17 January 2023 · Accepted: 10 March 2023 ·

Published Online: 3 April 2023




View Online



Export Citation



CrossMark

Natalí Guisande,¹  Monserrat Pallares di Nunzio,¹  Nataniel Martinez,²  Osvaldo A. Rosso,^{1,3} 
and Fernando Montani^{1,a)} 

AFFILIATIONS

¹Instituto de Física de La Plata (IFLP), Universidad Nacional de La Plata, CONICET CCT-La Plata, Diagonal 113 entre 63 y 64, La Plata 1900, Buenos Aires, Argentina

²Instituto de Física de Mar del Plata, Universidad Nacional de Mar del Plata & CONICET, Mar del Plata 7600, Buenos Aires, Argentina

³Instituto de Física, Universidade Federal de Alagoas (UFAL), BR 104 Norte km 97, 57072-970 Maceió, Brazil

Note: This paper is part of the Focus Issue on Ordinal Methods: Concepts, Applications, New Developments and Challenges.

^{a)}**Author to whom correspondence should be addressed:** f.montani@fisica.unlp.edu.ar

ABSTRACT

In this study, the Hénon map was analyzed using quantifiers from information theory in order to compare its dynamics to experimental data from brain regions known to exhibit chaotic behavior. The goal was to investigate the potential of the Hénon map as a model for replicating chaotic brain dynamics in the treatment of Parkinson's and epilepsy patients. The dynamic properties of the Hénon map were compared with data from the subthalamic nucleus, the medial frontal cortex, and a q -DG model of neuronal input-output with easy numerical implementation to simulate the local behavior of a population. Using information theory tools, Shannon entropy, statistical complexity, and Fisher's information were analyzed, taking into account the causality of the time series. For this purpose, different windows over the time series were considered. The findings revealed that neither the Hénon map nor the q -DG model could perfectly replicate the dynamics of the brain regions studied. However, with careful consideration of the parameters, scales, and sampling used, they were able to model some characteristics of neural activity. According to these results, normal neural dynamics in the subthalamic nucleus region may present a more complex spectrum within the complexity-entropy causality plane that cannot be represented by chaotic models alone. The dynamic behavior observed in these systems using these tools is highly dependent on the studied temporal scale. As the size of the sample studied increases, the dynamics of the Hénon map become increasingly different from those of biological and artificial neural systems.

Published under an exclusive license by AIP Publishing. <https://doi.org/10.1063/5.0142773>

An approach using information theory allows for the extraction of dynamical features from neurophysiological signals. In this paper, the dynamics of human intracranial electroencephalography (iEEG) are compared to two mathematical models: the Hénon map and a q -DG neural firing probability model. While the biological data present a much more complex spectrum of dynamical characteristics, the models are able to reproduce some aspects of neural dynamics.

I. INTRODUCTION

Dynamic systems describe processes that change over time. These models can be used to explain how symbolic properties emerge from physical and dynamic characteristics, which may also be an explanation for the emergence of mental qualities through neuronal activity.¹ A dynamic system can be stable, periodic, or chaotic. Chaotic systems are extremely sensitive to initial conditions and exhibit complex behaviors that become unpredictable in the

long term. Knowing the equation of a dynamic system can be useful for controlling it through conventional dynamic control methods. However, it can be challenging to identify patterns and determine their parameters when the equation is unknown, as is the case with electroencephalogram (EEG) signals.²

Many researchers in neuroscience have focused on studying chaotic patterns. In real biological dynamics, stable attractors are rare. Therefore, more complex behaviors (including oscillations and chaos) must be taken into consideration. This has led to the development of various numerical techniques for analyzing complex time series, which can be used to describe dynamic processes at both the temporal scale of cerebral dynamics and the fluctuations of clinical symptoms.¹ Applying these methods to physiological data has shown that complex behaviors are associated with healthy states, while simple dynamics are associated with pathological cases.³ There are even studies that support the concept of “dynamic disease,”^{4,5} which refers to pathological states characterized by changes in physiological rhythms.¹

Previous studies have indicated that brain waves exhibit chaotic behaviors. While solid evidence of chaos in cerebral dynamics (from a mathematical perspective) has only been found at the level of axons and individual and paired cells, the results suggest that it is possible for brain signals to be distributed according to chaotic patterns at all levels of its hierarchy.^{6–8}

The brain is a highly complex dynamic system, and it is not fully understood how it processes information and generates behavior. The use of mathematical models, such as chaotic functions, can help to study and understand the complex dynamics of the brain and how it works. Several contemporary studies in the field of biology have shown that certain well-known chaotic systems, such as the Logistic Map, Lorenz, and Rössler systems, can accurately describe the chaotic dynamics of biological systems under certain conditions, that is, specific parameter values.⁸ One example of these types of chaotic systems is the Hénon map, which is a mathematical function that exhibits complex and chaotic behavior.⁹ It has been proposed as a potential tool for studying and modeling brain activity and has been used to train artificial neural networks and study their similarities to biological brain networks and their chaotic behavior.^{2,10}

By analyzing the behavior of the Hénon map and comparing it to brain activity, it may be possible to obtain information about the principles governing brain function and develop new approaches to treating neurological conditions. In addition, the complexity and unpredictability of chaotic functions may be useful for understanding how the brain processes and responds to stimuli and how it adapts to changes in its environment.

The goal of this study is to use information theory tools to compare the cerebral dynamics of the subthalamic nucleus with those of the Hénon map and a dichotomized q -Gaussian neuronal firing model. The latter is capable of generating spike trains from a population of neurons, which is useful for characterizing the local behavior of the network. The purpose of this investigation is to determine whether there are similarities between the dynamics of these models that could be utilized in future studies of neurodegenerative diseases like Parkinson's and Alzheimer's. Previous research has suggested that chaotic dynamics may be associated with healthy states of brain dynamics, while non-chaotic dynamics may be associated with

pathological states. Therefore, the primary objective of this work is to establish whether the dynamics of the models mentioned display similarities, and whether these similarities can be used to advance future research on the subject.

A. Comparing the dynamics of the Hénon map and neural activity for noninvasive brain stimulation of Parkinson's and epilepsy patients

The subthalamic nucleus (STN) of the basal ganglia has been identified as a decision gatekeeper in human patients who have had electrodes implanted for clinical deep-brain stimulation (DBS) treatment. The STN is thought to set the decision threshold when there is contradictory information by postponing action until the issue is resolved.^{11,12} Motor symptoms of movement disorders, such as Parkinson's disease, can be effectively treated by STN-DBS. However, it is also known to have a subtle but significant negative impact on behavior, mood, and cognition, with impulsivity being its most common symptom.^{13,14}

Different noninvasive brain stimulation (NIBS) technologies are currently being studied as potential future strategies for the treatment of Parkinson's disease (PD). In addition to being used to investigate brain physiology, NIBSs are also being recognized for their therapeutic potential as a supplementary treatment for a variety of neurological and psychiatric disorders.^{15,16}

Understanding brain dynamics is necessary for the therapeutic treatment of several neurological diseases, such as Parkinson's and epilepsy. These therapeutic options now have a strong experimental foundation, but lack a solid theoretical foundation. In addition, many long-term effects of brain stimulation on cerebral neuronal networks are unknown. The dynamic behavior of discharge activity patterns is important because they are closely related to the physiological manifestation of neurons.

The analysis of chaotic systems is a central part of the study of deep-brain stimulation. Several studies suggest that it is convenient to analyze the nonlinear dynamics of biological systems using chaos theory as a means of computation.¹⁷ Data analysis using formal models is consistent with the idea that signals in the brain exhibit chaotic patterns at all levels.⁸ Furthermore, EEG analysis exhibits chaotic patterns and bifurcations, supporting the idea that chaos exists in these types of signals.¹⁸

The Hénon map is among the best-known instances of chaotic behavior in nonlinear dynamical systems. This translates a point (x_n, y_n) on the plane to a new point for succeeding steps. The comparison of the dynamics between the Hénon map and neural activity is interesting, especially considering the recent proposal to use the Hénon map to simulate chaotic brain dynamics in the noninvasive stimulation of patients with Parkinson's disease and epilepsy.⁹ To study the temporal dynamics of Hénon, the Bandt and Pompe methodology was used to calculate the Shannon entropy, statistical complexity, and Fisher Information of the map time series.

The system dynamics were analyzed by comparing these findings to actual local field potential (LFP) data from the subthalamic nucleus (STN), medial frontal cortex (MFC), and a dichotomized q -Gaussian theoretical model used to simulate spike trains of highly correlated neuronal populations. More specifically, time series generated by the LFPs were used to analyze the differences

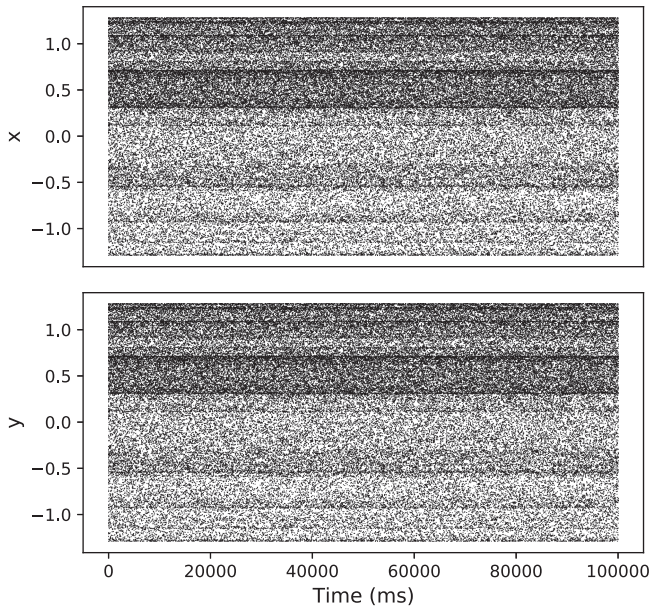


FIG. 1. Temporal evolution in milliseconds of the coordinates x and y of the two-dimensional Hénon map.

and similarities with the Hénon Map and compared with the q -DG model, which takes into account higher order correlations in both input and output statistics.¹⁹ Representing these complex systems by simulated or experimental time series can provide a better way to visualize the hidden patterns related to network dynamics.

II. METHODS

A. Topological background

1. The Hénon map: A model for chaotic dynamics

The classical Hénon map is defined by the following coupled equations:

$$\begin{cases} x_{n+1} = 1 - ax_n^2 + y_n, \\ y_{n+1} = bx_n. \end{cases}$$

Using $a = 1.4$ and $b = 0.3$ as parameters, the system exhibits irregular behavior that progresses into a chaotic attractor.^{9,10,20} The Hénon map was used to generate two one-dimensional time series representing the position of the x and y coordinates (Fig. 1). These time series were then assigned a probability using the Bandt–Pompe (BP) method²¹ and the information-theoretic quantifiers were calculated. The results of both components were averaged to obtain the final values. The aim of this simulation was to mimic the dynamics of neuronal activity using the Hénon map.

2. Modeling neural correlations using the dichotomized q -Gaussian model

The dichotomized q -Gaussian model (q -DG) is a model of neural activity that involves thresholding a multivariate q -Gaussian

random variable to produce a series of action potentials or spike trains. The correlations among neurons in this model arise from correlations in the underlying q -Gaussian distribution. The q -DG model generalizes Amari’s dichotomized Gaussian model to account for higher-order correlations in both the input and output statistics of neurons. The deformation parameter, q , represents the heavy tails of the q -Gaussian distribution.^{22–27} The joint firing probability density of an N -neuron population can be expressed in terms of the T-Student (T) distribution, as shown in Eq. (1),

$$f(r) = \zeta \sqrt{\frac{1-\alpha}{\alpha}} \left[1 + \frac{(T^{-1})^2}{\nu} \right]^{\frac{\nu+1}{2}} \times \exp \left[-\frac{\zeta}{2} \frac{1-\alpha}{\alpha} \left(T^{-1} - \frac{h}{\zeta \sqrt{1-\alpha}} \right)^2 \right]. \quad (1)$$

Here, ζ is a scale factor defined as $\zeta = \sqrt{\frac{5-3q}{3-q}}$, $r = \frac{k}{N}$, $\nu = \frac{3-q}{q-1}$ and k represents the population spike count distribution. Note that T^{-1} is the inverse cumulative distribution function for a T-Student’s with degrees of freedom ν . At any given time, r represents the fraction of neurons within the population that are spiking. Overall, the equation shows that $f(r)$ is determined by the values of α , h , q , and ν , which together determine the T-Student distribution.

The q -DG model was selected due to its simplicity in numerical implementation. By varying the input correlation coefficient α , the mean value h , and the deformation parameter q , it is possible to generate spike trains for a population by determining the fraction of the population that is spiking at each time, while taking into account the correlations in the input and output signals of the population. These spike trains can be superimposed to obtain a signal of the local behavior of the neural network, which can be compared with the LFPs from experimental data. To construct the time series of spike trains, a Monte Carlo simulation with N neurons is implemented using the joint firing probability density to obtain the fraction of the population spiking. At each time point, the percentage of total spiking neurons is calculated, and a random process is used to determine which neurons will spike. This process is repeated for all time steps to simultaneously construct all spike trains. Finally, the spike trains are summed time by time to obtain a single global (local) variable. Figure 2 demonstrates this approach, showing spike trains with $N = 30$ neurons, $h = 1$, and $q = 1.1$ generated using the model with input correlation coefficient values of $\alpha = [0, 0.25, 0.51, 0.80]$ adjusted to output correlation values of $\rho = [0, 0.1, 0.25, 0.5]$. More details regarding the relationship between input correlations α and output correlations ρ can be found in the following papers: Refs. 22–27.

3. The Bandt–Pompe approach to examining ordinal structure and quantify information

The Bandt–Pompe (BP) technique^{21,28–30} is employed to estimate the underlying probability distribution function (PDF) of a time series $\chi(t) = \{x_i; t = 1, \dots, M\}$, which is a collection of M measurements of the observable χ . The method involves the transformation of the time series into symbolic sequences and the identification of ordinal structures in the data by considering all possible permutations of the values of the series in fixed-size windows. This

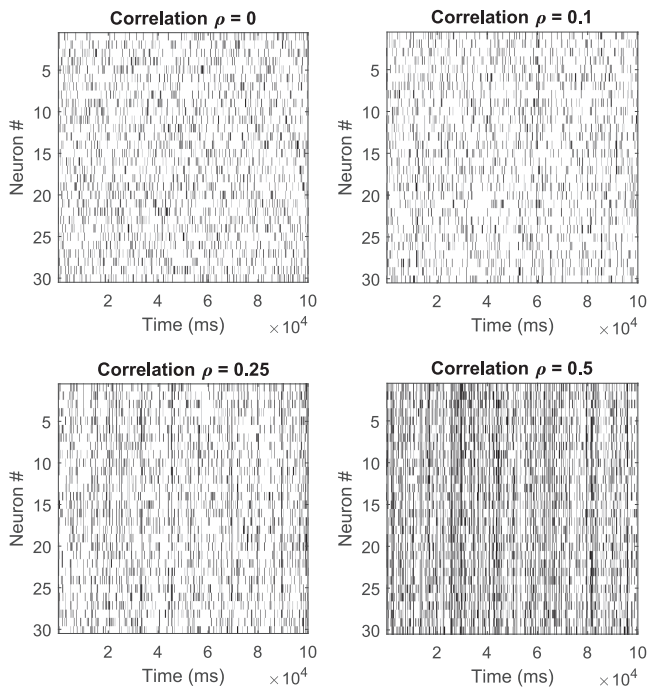


FIG. 2. The asymptotic joint firing probability density can be used to generate different sets of spike trains by varying the input correlation coefficient α , the mean value h , and the deformation parameter q . Although the figure shows the evolution of the parameter ρ , which is the output correlation coefficient, it is worth noting that its relationship with the input correlation coefficient α is determined by the choice of the remaining parameters.

process results in a probability distribution of ordinal patterns, derived from the histogram of causal patterns in the signal, that can be utilized to compute various information theory quantifiers. These quantifiers offer insight into the dynamic characteristics of the system represented by the time series.

Once an embedding dimension D and a time delay τ are fixed, the time series is partitioned into $n = M - (D - 1)\tau$ overlapping segments, each consisting of $D > 1$ observations separated by $\tau \geq 1$. Each partition is represented as^{31,32}

$$(s) \mapsto (x_{s-(D-1)\tau}, x_{s-(D-2)\tau}, \dots, x_{s-\tau}, x_s), \quad (2)$$

creating a D -dimensional vector of values at each time $s, s - \tau, \dots, n$. As D increases, more previous data are included in the vectors. For each partition, the permutation $\pi = (r_0, r_1, \dots, r_{D-1})$ of the index numbers $(0, 1, \dots, D - 1)$ is determined. The permutation of the index numbers defined by the inequality is

$$x_{s-r_{D-1}\tau} \leq x_{s-r_{D-2}\tau} \leq x_{s-r_1\tau} \leq \dots \leq x_{s-r_0\tau}. \quad (3)$$

All $D!$ possible permutations π_i of order D are considered. In cases of ambiguity, it is proposed that $r_i < r_{i-1}$ if $x_{s-r_i\tau} = x_{s-r_{i-1}\tau}$. Note that the symbolic sequence $\{\pi_i\}_{i=1, \dots, n}$ is an ordinal symbolic sequence.

The relative frequency for each π_i is determined as follows:

$$p_j(\Pi_j) = \frac{\text{number of partitions of type } \Pi_j \text{ in } \pi_i}{n}, \quad (4)$$

where Π_j represents each one of the $D!$ different ordinal patterns. It is important to note that Π_j represents a specific ordinal pattern for a partition, while π_i represents the sequence of all ordinal patterns obtained from all partitions in the time series. Therefore, the probability distribution P is calculated based on the frequency of each specific Π_j within the entire sequence $\pi_i: P = \{p_j(\Pi_j)\}_{j=1, \dots, D!}$. The condition $M \gg D!$ must be met to apply this technique.²¹ A brief example is presented below to illustrate the method explained. Consider the time series $\chi(t) = \{10, 13, 15, 12, 20, 18, 25\}$ with $M = 7$. The Bandt and Pompe methodology with $D = 3$ and $\tau = 1$ is applied to evaluate the PDF. The vectors $(10, 13, 15), (13, 15, 12),$ and $(15, 12, 20)$ are represented by the ordinal pattern $\{012\}$, while $(12, 20, 18)$ is represented by $\{120\}$ and $(20, 18, 25)$ is represented by $\{201\}$. From the permutation of the embedding dimension, the number of possible states is $D! = 6$. The probabilities of occurrence associated with each mutually exclusive permutation are given by $p(\{012\}) = p(\{120\}) = p(\{201\}) = 2/5$ and $p(\{021\}) = p(\{102\}) = p(\{210\}) = 0$. These results form the PDF $P = \{p_1, p_2, p_3, p_4, p_5, p_6\}$ associated with the time series χ . For more examples of how to implement this methodology, please refer to Ref. 32.

The BP approach is used to determine PDF of a time series, which is then used to compute Shannon entropy as a measure of the information content of the signals. This method provides insights into the causality of the signal that a basic histogram cannot offer, as the PDF is derived from the histogram of causal patterns. It is worth noting that since the estimated PDF P is derived from a histogram, it is discrete. When the probability distribution of ordinal patterns is used to calculate Shannon entropy, it is referred to as permutation Shannon entropy.

It should be noted that randomness metrics do not fully capture the presence of ordinal structures in a process. For a more accurate characterization of the dynamics of the system represented by its time series, measures of statistical or structural complexity are required, as discussed in Ref. 33.

In this context, the BP methodology is employed to estimate the underlying PDF of a time series $\chi(t)$ and to calculate several information-theoretic quantifiers. The ordinal patterns method is applied to detect and quantify the presence of ordinal structures in the time series, for the purpose of comparing the dynamics of human brain physiological signals with mathematical models using the BP method. Using the resulting probability distribution, various information-theoretic quantifiers such as Shannon entropy, statistical complexity, and Fisher information can be calculated. These quantifiers offer valuable insights into the dynamics of the system represented by the time series and can facilitate the comparison between human brain physiological signals and mathematical models.

In the discrete case, the Shannon entropy of a time series with a corresponding probability distribution $P \equiv \{p_j\}_{j=1, \dots, N}$ is given by³⁴

$$S[P] = - \sum_{j=1}^N p_j \log_2(p_j), \quad (5)$$

where N is the number of possible states of the physical system under consideration and p_j is the probability of each state. When it is certain which of the potential outcomes, represented by j , will occur, with probabilities given by $P_0 = \{p_{j^*} = 1 \text{ and } p_j = 0 \text{ for all } j^* \neq j\}$, the Shannon entropy is zero, indicating that our understanding of the process is maximized. On the other hand, when the probability distribution is uniform, with $P_e = p_j = 1/N, \forall j = 1, \dots, N$, our knowledge is negligible. It is worth noting that large changes in P that occur over a small range have little impact on the Shannon entropy, as it is a “global” measure.

Perfect order and maximal unpredictability are opposite extremes, with neither having any structure. In these cases, the complexity C should be zero, as shown by $C[P_0] = C[P_e] = 0$, where P_0 is the probability distribution of the maximally disordered system and P_e is the probability distribution of the perfectly ordered system. It has been shown that the range of feasible values of C lies between a minimum of C_{\min} and a maximum of C_{\max} , constraining the possible values of the statistical complexity to a specific entropy–complexity plane.³⁵ The statistical complexity is a measure that captures useful differences in the dynamics of the systems under study. This metric was developed as a result of the pioneering work of L’opez-Ruiz *et al.*³⁶ In this study, the version of the metric developed by Martin–Rosso–Plastino, also known as MPR complexity,^{35,37} will be utilized. Whenever the term “complexity” is used, it will be referring to this specific metric. The statistical complexity is given by

$$C_{JS}[P] = \mathcal{Q}_J[P, P_e] \cdot H[P], \tag{6}$$

where H is the normalized Shannon entropy defined by $H[P] = \frac{S[P]}{S_{\max}}$ with $S_{\max} = S[P_e] = \log_2 N$ and $0 \leq H \leq 1$. The disequilibrium \mathcal{Q}_J is given as a function of the Jensen–Shannon divergence,

$$\mathcal{Q}_J[P, P_e] = Q_0 \mathcal{J}[P, P_e], \tag{7}$$

where the Jensen–Shannon divergence is defined as

$$\mathcal{J}[P, P_e] = H\left[\frac{P + P_e}{2}\right] - \frac{H[P]}{2} - \frac{H[P_e]}{2}. \tag{8}$$

The normalization constant Q_0 ensures that $0 \leq \mathcal{Q}_J \leq 1$. It is the inverse of the highest possible value of $\mathcal{J}[P, P_e]$, which is obtained when one component of P , such as p_m , is equal to one and the remaining p_j are equal to zero.

The Jensen–Shannon divergence, a metric for comparing the difference between probability distributions, is often used for analyzing the symbolic structure of different sequences.³⁸ The statistical complexity measure (SCM) relies on two probability distributions: the distribution representing the system being analyzed, P , and the uniform distribution, P_e .^{28,30,35,39}

In contrast to Shannon’s entropy, Fisher’s information is sensitive to local changes.^{40,41} It is defined as

$$F[f] = \int \frac{|\vec{\nabla} f(x)|^2}{f(x)} dx. \tag{9}$$

This measure represents the gradient content of the distribution f (a continuous PDF) and is, therefore, highly sensitive to even small, localized perturbations. Fisher’s Information can be interpreted in several ways: as a measure of the ability to estimate a parameter, as the amount of information that can be extracted from a set of

measurements, and as a measure of the level of disorder in a system or phenomenon.^{41,42} Its most important property is known as the Cramer–Rao bound. It is worth noting that the gradient operator plays a significant role in determining the contribution of small, local f variations to the Fisher information value, making it a “local” measure. In contrast to Shannon entropy, which decreases with a skewed distribution, Fisher information increases in such cases. The ability to detect local changes is useful in situations where a concept of “order” is relevant.^{43–45} The issue of Information loss due to discretization has been extensively studied (see, for example, Refs. 46–48 and their references). In particular, it involves the loss of Fisher’s shift-invariance, which is not relevant for our present purposes.

The calculation of Fisher’s Information was performed using the method proposed by Sanchez-Moreno *et al.*,⁴⁹ which is based on the probability amplitude $f(x) = \psi(x)^2$. The equation for this is

$$F[\psi] = 4 \int \frac{d\psi^2}{dx} dx. \tag{10}$$

The discrete, normalized version of this ($0 \leq F \leq 1$) is given by

$$F[P] = F_0 \sum_{i=1}^{N-1} (\sqrt{p_{i+1}} - \sqrt{p_i})^2. \tag{11}$$

The normalization constant F_0 is defined as follows:⁴⁵

$$F_0 = \begin{cases} 1 & \text{if } p_{i^*} = 1 \text{ for } i^* = 1 \text{ or } i^* = N \text{ and } p_i = 0 \forall i \neq i^*, \\ 1/2 & \text{otherwise.} \end{cases} \tag{12}$$

It is worth noting that the general behavior of Fisher’s Information measure is opposite to that of Shannon’s entropy.⁵⁰ When the system is in a highly ordered state, it can be described using a PDF represented by $P_0 = \{p_k \cong 1; p_i \cong 0 \forall i \neq k; i = 1, \dots, N\}$ (with N being the number of states in the system), resulting in a normalized Fisher’s Information measure of $F[P_0] \cong F_{\max} = 1$ and a Shannon entropy of $S[P_0] \cong 0$. On the other hand, if the system being analyzed is in a highly disordered state, it is reasonable to assume that it is defined by a PDF represented by the uniform distribution $P_e = \{p_i = 1/N \forall i = 1, \dots, N\}$, which yields $S[P_e] \cong S_{\max}$ and $F[P_e] \cong 0$.

B. Comparing time series dynamics using the complexity–entropy causality plane

The Shannon entropy–statistical complexity plane by Martin, Plastino, and Rosso allows for the comparison of similar time series dynamics through subtle characteristics of the system’s dynamics. This is achieved by calculating the Shannon entropy and statistical complexity of the time series and then plotting the results on a two-dimensional plane.

Shannon entropy measures the amount of information contained in a time series and statistical complexity measures the amount of structure and patterns present in the time series. By plotting these two values on a plane, it is possible to compare the dynamics of similar time series and see if they exhibit similarities or differences in terms of entropy and complexity.

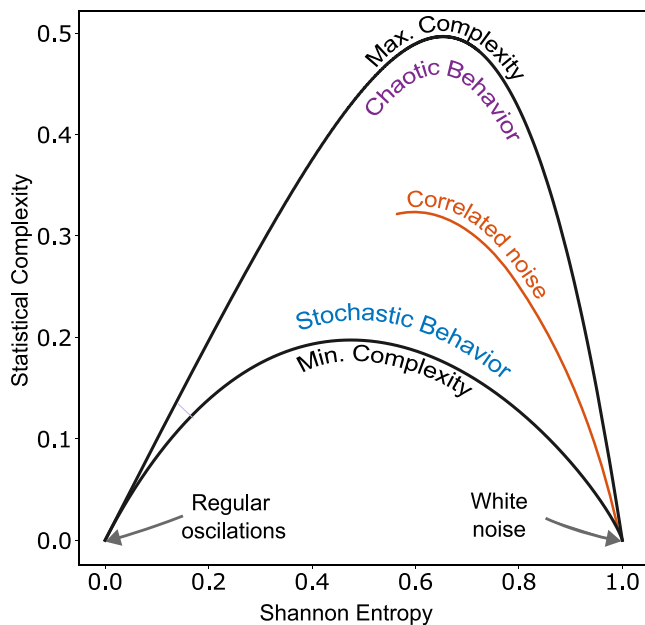


FIG. 3. Complexity–entropy causality plane: this plot depicts the relationship between complexity and entropy in a time series. The maximum and minimum complexity bounds are plotted, with chaotic systems located toward the maximum complexity. These systems have entropies between 0.45 and 0.7 and complexities close to the maximum. Stochastic systems are located near the minimum complexity curve. The middle region represents correlated noise, while stochastic behaviors can be found below this region. The regions of white noise and regular oscillations are also shown. The plot is generated by calculating the Shannon entropy and statistical complexity of a time series using an embedding dimension of $D = 6$.^{51,52}

This method is useful for analyzing complex systems and detecting patterns or changes in the system’s dynamics over time. It can also be used to compare different dynamic systems and see if they exhibit similarities or differences in terms of entropy and complexity.

As seen in Fig. 3, in the entropy complexity plane, the maximum and minimum complexity bounds are plotted, which are determined by the embedding dimension used to calculate the PDF. In the middle, correlated noise (color noise) is located (with medium complexity and medium–high entropy values). Stochastic behaviors are found below correlated noise. Chaotic systems are located toward the maximum complexity (with entropies between 0.45 and 0.7, and complexities close to the maximum, due to their internal correlation structures). Stochastic systems are located near the minimum complexity curve. The regions of white noise (with maximum entropy and minimum complexity) and regular oscillations (with minimum complexity and entropy both) are also observed.^{51,52}

C. Neurophysiological data

In this study, the chaotic dynamics of the Hénon map were compared with brain dynamics, specifically in the subthalamic nucleus (STN) region where deep-brain stimulation is implemented. The aim was to determine if it was possible to emulate brain

dynamics using the Hénon map. However, only pathological intracranial data from the STN region were available for comparison. Therefore, another brain region was selected to contrast the results, as it was possible that the activity in this region would be less chaotic than that of healthy patients. Several brain regions were considered for this purpose, including the thalamus, which is important in sensory integration and movement modulation, and the prefrontal cortex, which is important in decision making and cognitive processing. The medial frontal cortex was ultimately chosen because it was the region with the most similar activity for which local field potential (LFP) data were available. Two sets of experimental data were used in this study to analyze the dynamics of the brain. One set was collected from the STN region and the other from the medial frontal cortex (MFC). The STN data were obtained from patients with Parkinson’s disease and included pathological LFP activity, while the MFC data were collected from healthy regions of individuals with refractory epilepsy and may provide a reference for normal LFP activity. The invasive procedure of introducing electrodes into the brain was used to record the LFP activity in both regions. The inclusion of data from both the STN and MFC allowed for a comparison of normal and pathological LFP activity, providing a deeper understanding of brain dynamics.

1. Pathological LFP activity in the STN region

Since the Hénon map was proposed to stimulate patients with Parkinson’s disease, it was decided to contrast the dynamic behavior of the Hénon map with the brain dynamics of the stimulated region in this type of patient: the subthalamic nucleus (STN). For this purpose, the dynamics of the local field potentials (LFPs) of the STN were studied in human patients. The sequential conflict task human LFP recordings were collected from an Oxford University database.^{11,53}

The data for this study were obtained from a database containing records from 15 patients diagnosed with Parkinson’s disease. These patients had undergone electrode implantation for deep-brain stimulation treatment, allowing for intracranial recordings of the STN region. Of the patients included in the study, 11 had Medtronic 3389 electrodes and 4 had Boston Vercise directional leads. Results from three patients were excluded due to incorrect task execution or lack of sufficient channels for analysis. During the experiment, participants were shown a series of images of a mouse facing either left or right. Cues were presented for 200 ms with an interstimulus interval of 600 ms, resulting in an 800 ms interval between onsets. Participants were asked to judge the direction in which the mouse would “run” based on probabilities extracted from a series of sequential cue images and then respond accordingly. Responses were made by pressing a button with the thumb of the congruent hand after viewing a self-chosen number of cues, when the participant felt they had sufficient evidence to make a decision. Prior to recording, participants underwent a brief training session where they were first asked to respond only after seeing a set number of stimuli and were then informed that for the main experiment, they could decide how many stimuli to observe themselves. For the analysis, data from 13 patients were considered. Three right STN channels and three left channels were used, with 100 different stimuli analyzed for each of these channels. Temporal windows of

200 and 400 ms were chosen in order to implement an embedding dimension of $D = 3$ and $D = 4$ in the BP methodology. Each individual signal had a length of 800 ms and was downsampled to a frequency of 150 Hz. For the analysis in this study, raw data from all patients were utilized.

2. Normal LFP activity in the MFC region

For this study, data from the MNI Open iEEG Atlas, a database of recordings of normal brain activity from intracranial electrodes, were used. The recordings were taken from the atlas and corresponded to a state of quiet wakefulness with closed eyes. They were used to compare data from the subthalamic nucleus with healthy regions. The source data were collected from epileptic patients with an unidentified focus of epilepsy using intracranial electrodes, with each patient's channels corresponding to normal regions outside the epileptic zones. The dataset included 1785 channels with normal neural activity from 106 patients. To compare patient activity, the electrodes were placed in a common stereotactic space, allowing for the accumulation and superposition of results from a large number of subjects.^{54–56}

In this work, Dixi intracerebral electrodes (labeled as “D” in the database) were used to record data from the medial frontal cortex (region 19). These data were included in order to contrast the LFP data from STN patients with Parkinson's disease with data from a healthy region that may have similar neuronal activity characteristics. The length of the signals was 68 s, and they were sampled at a rate of 200 Hz.

D. Optimizing the temporal window size for analyzing dynamics with embedding dimension D

Small temporal windows were selected for the analysis in this study based on insights from the research of Panzeri *et al.* titled “The Role of Spike Timing in the Coding of Stimulus Location in Rat Somatosensory Cortex.”⁵⁷ This research aimed to measure the

amount of information conveyed by both spike counts and spike times during a specific post-stimulus time window (0-T). The study findings suggest that longer time windows lead to a decrease in spike count information, which is related to the size of the bin used in the calculations. Decreasing the bin size, on the other hand, results in an increase in information.

The size of the selected embedding dimensions is closely tied to the size of the implemented temporal windows, where $M \gg D!$. A D value of 1 does not provide causal information, and a value of 2 provides only minimal information. Therefore, the embedding dimensions of interest are those where $D > 3$. However, some of the signals are very short, which precludes consideration of $D > 4$ due to statistical significance. Additionally, it is worth noting that the temporal windows were chosen contiguously without any overlap between them.

In the results section of this paper, the minimum temporal window for applying an embedding dimension of $D = 3$ is determined by the MFC data series, which have a number of samples $M = 13\,600$ representing a duration of 68 s. Since $M \gg D!$ is required to implement the BP methodology, the smallest window implemented is 200 ms, which is obtained by considering windows of $M = 40$. This translates to a window of $M = 75$ when considering 200 ms in the STN data. For the theoretical models, it was fixed that $M = 40$ corresponds to 200 ms. It should be noted that the Hénon map moves toward the chaotic region in the complexity–Shannon entropy plane as the number of samples considered increases, while in the q -DG model, noise components increase causing it to move toward the lower right corner. In the case of $D = 4$, the window is considered to be 400 ms, with values being doubled in each case.

III. RESULTS

First, the time series to be analyzed were determined. From the experimental data, the unfiltered STN and MFC LFPs were considered, and for the Hénon map, the x and y coordinate positions

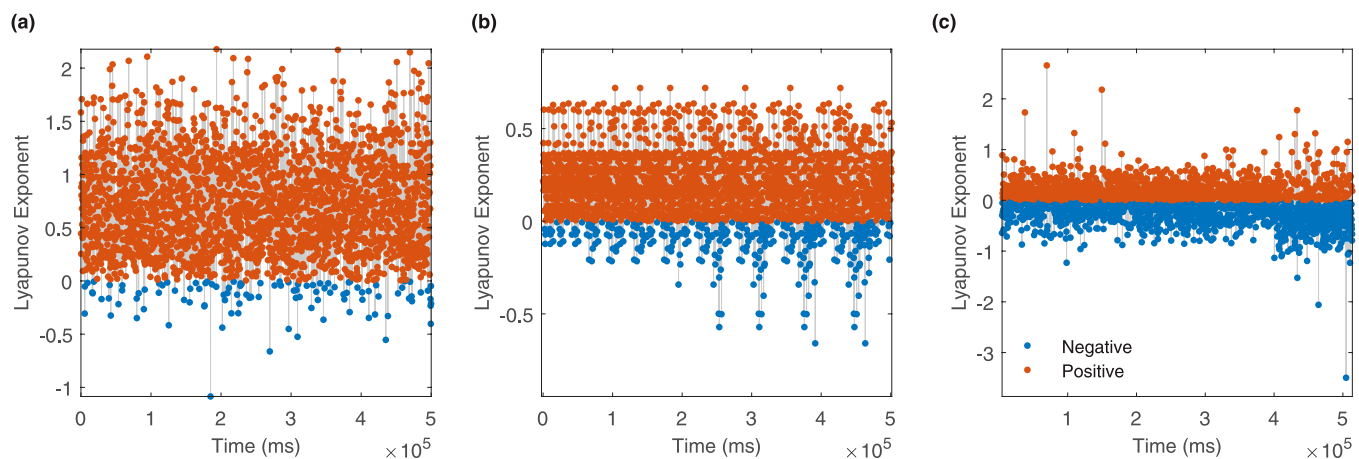


FIG. 4. Lyapunov exponents for a 200 ms time window: (a) corresponds to the Hénon map, (b) shows 800 ms STN LFP signals calculated individually and then overlaid the exponents in a single vector, and (c) corresponds to the Lyapunov exponents calculated on 68 000 ms MFC LFP signals, which were also overlaid in a single vector.

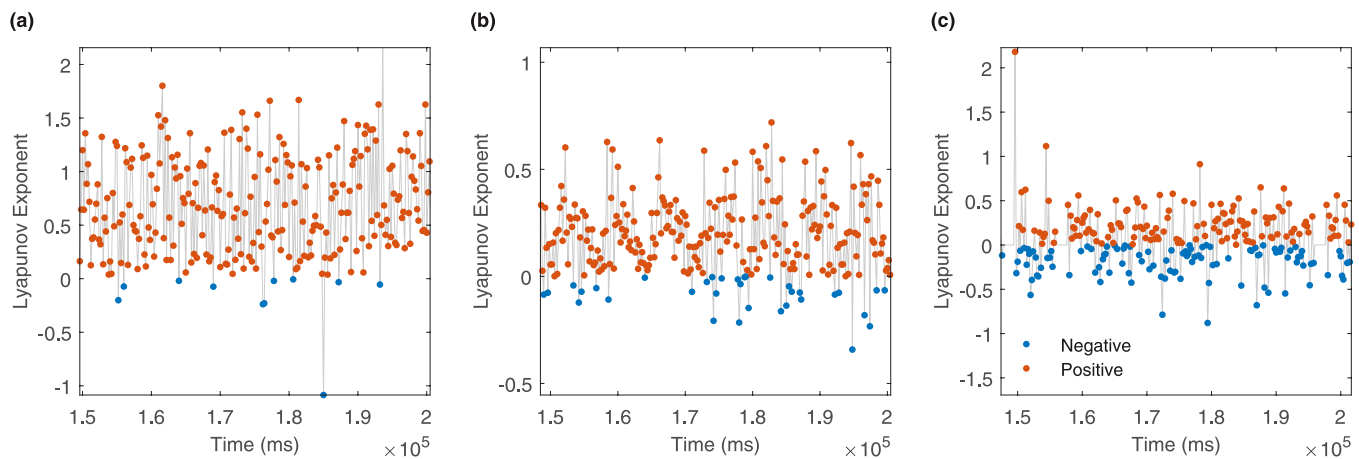


FIG. 5. Lyapunov exponents for a 200 ms time window: Zoomed-in on the region between 1.5×10^5 and 2.0×10^5 ms. (a) corresponds to the Hénon map, (b) shows 800 ms STN LFP signals calculated individually and then overlaid the exponents in a single vector, and (c) corresponds to the Lyapunov exponents calculated on 68 000 ms MFC LFP signals, which were also overlaid in a single vector.

(two time series) were considered. For the dichotomized q -Gaussian model, the sum of the trains of spikes of all neurons was considered as the time series in order to imitate the behavior of the LFPs that consider the global behavior of a given region.

Next, each time series was divided into small windows for each case. The smallest implemented windows were 200 ms to have good statistics in the BP dimension $D = 3$. For $D = 4$, a window of 400 ms was implemented. Several dimensions were tested, but this was where the different quantifiers were best appreciated. Additionally, the length of the STN experimental data time series did not allow for the analysis of dimensions greater than $D = 4$ (remember that $D > M!$).

The chaos level of the systems was analyzed using Lyapunov exponents, which can then be used to search for possible stabilities or chaos. The figures show the Lyapunov exponent for the Hénon map when considering a window of 40 and 80 steps in the model (which were fixed to correspond to 200 and 400 ms, respectively). Figure 4 shows the Lyapunov exponents for a 200 ms time window. Figure 4(a) corresponds to the Hénon map, while Fig. 4(b) shows the exponents calculated on 800 ms STN LFP signals that were overlaid in a single vector. Figure 4(c) corresponds to the Lyapunov exponents calculated on 68 000 ms MFC LFP signals, which were also overlaid in a single vector. Figure 5 is a zoomed-in version of Fig. 4 for the region between 1.5×10^5 ms and 2.0×10^5 ms.

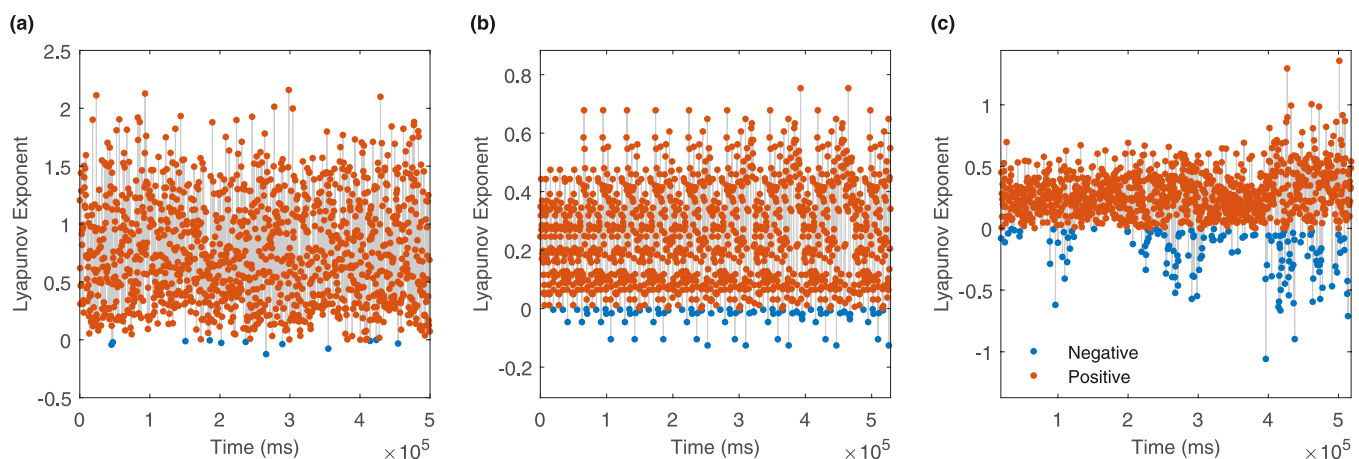


FIG. 6. Same as Fig. 6, but with a 400 ms time window.

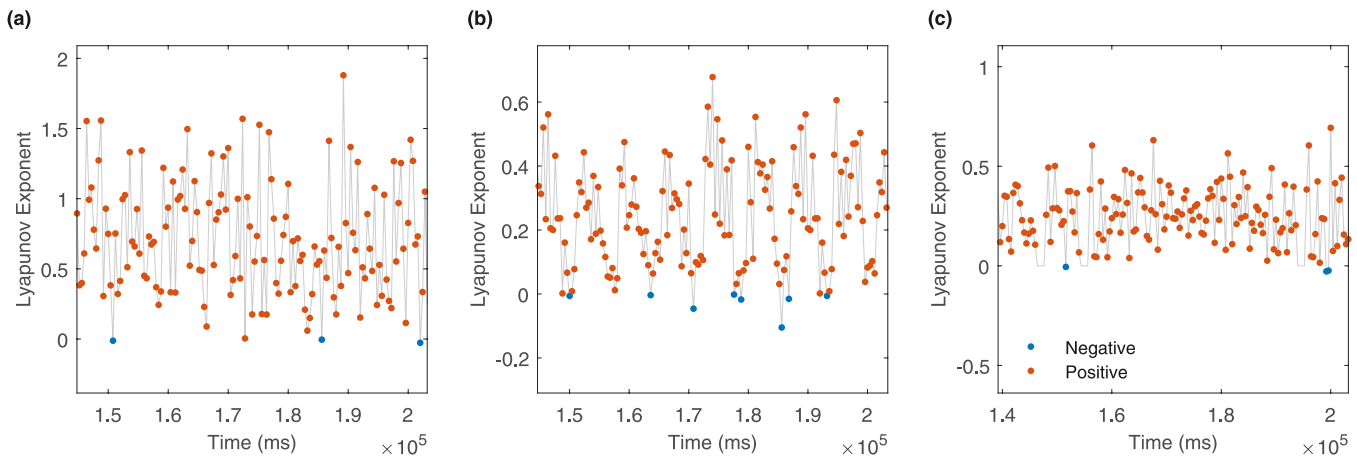


FIG. 7. Same as Fig. 7, but with a 400 ms time window.

Figures 6 and 7 are similar to Figs. 4 and 5, respectively, but with a 400 ms time window.

Note that positive Lyapunov exponents show divergence and chaos, while negative exponents show convergence. Therefore, it is a measure of the speed at which infinitely close trajectories converge or diverge. The Bandt–Pompe method was used to calculate the Shannon entropy, statistical complexity, and Fisher information for each temporal window and obtain the probability distributions of the series. For the Hénon map, these quantifiers were calculated as the average value obtained for each coordinate. Figure 8 compares the dynamics of the STN and the Hénon map. The plot

shows Shannon entropy, statistical complexity, and Fisher information calculated on LFPs with a temporal window of 200 ms and an embedding dimension of Bandt and Pompe $D = 3$. The blue points represent data from the STN, while the light blue points represent data from the Hénon map. Figure 9 is similar to Fig. 8, but with a BP dimension $D = 4$ and a temporal window of 400 ms.

Figure 10 compares the dynamics of the MFC and the STN. The plot shows Shannon entropy, statistical complexity, and Fisher information calculated on LFPs with a temporal window of 200 ms and an embedding dimension of Bandt and Pompe $D = 3$. The violet points represent data from the MFC, while the blue represents

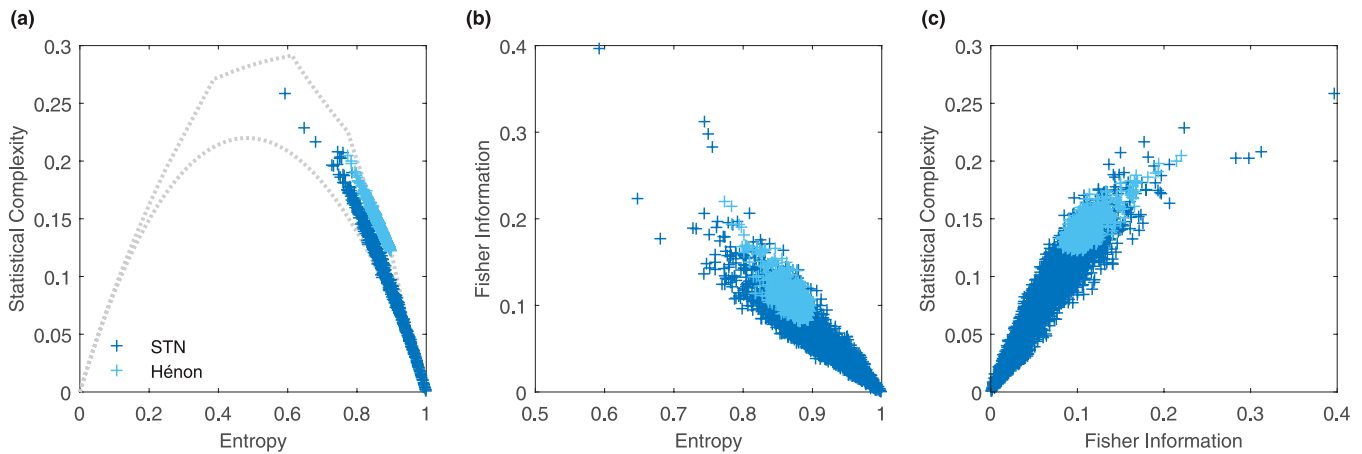


FIG. 8. Comparison of dynamics in the subthalamic nucleus (STN) and the Hénon map using $D = 3$. Shannon entropy, statistical complexity, and Fisher information calculated on local field potentials (LFPs) using an embedding dimension of Bandt and Pompe $D = 3$ and a temporal window of 200 ms. Blue represents data from the STN and light blue represents data from the Hénon map. (a) Complexity–entropy causality plane. (b) Shannon entropy–Fisher information plane. (c) Statistical complexity–Fisher information plane.

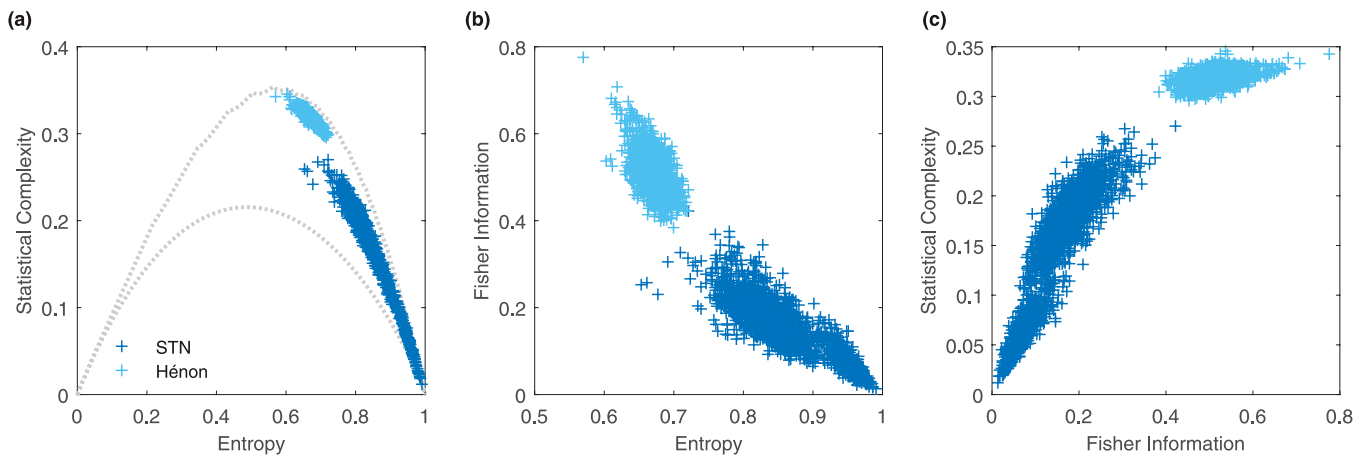


FIG. 9. Same as Fig. 8, but with a BP dimension $D = 4$ and a temporal window of 400 ms.

data from the STN. Figure 11 is similar to Fig. 10, but with a BP dimension $D = 4$ and a temporal window of 400 ms.

Figure 12 compares the dynamics of the MFC and the Hénon map. The plot shows Shannon entropy, statistical complexity, and Fisher information calculated on LFPs with a temporal window of 200 ms and an embedding dimension of Bandt and Pompe $D = 3$. The violet points represent data from the MFC, while the light blue points represent data from the Hénon map. Figure 13 is similar to Fig. 12, but with a BP dimension $D = 4$ and a temporal window of 400 ms. In Figs. 14 and 15, the dichotomized q -Gaussian model is implemented with parameters $q = 1.1$, $\rho = 0.1$, and $h = 0.1$ for the q -parameter, covariance, and mean, respectively. The plots compare the dynamics of the Hénon map and the dichotomized q -Gaussian model, with the light blue points representing data from the Hénon

map and the orange points representing data from the dichotomized q -Gaussian model. In Fig. 14, the plots are generated using an embedding dimension of Bandt and Pompe $D = 3$ and a temporal window of 200 ms, while in Fig. 15, these values are $D = 4$ and 400 ms, respectively.

IV. DISCUSSIONS

In Fig. 4, Lyapunov exponents for a 200 ms time window are shown. Figure 4(a) corresponds to the Hénon map, Fig. 4(b) shows 800 ms STN LFP signals calculated individually and then overlaid the exponents in a single vector, and Fig. 4(c) corresponds to the Lyapunov exponents calculated on 68 000 ms MFC LFP signals, which were also overlaid in a single vector. In Fig. 5, which

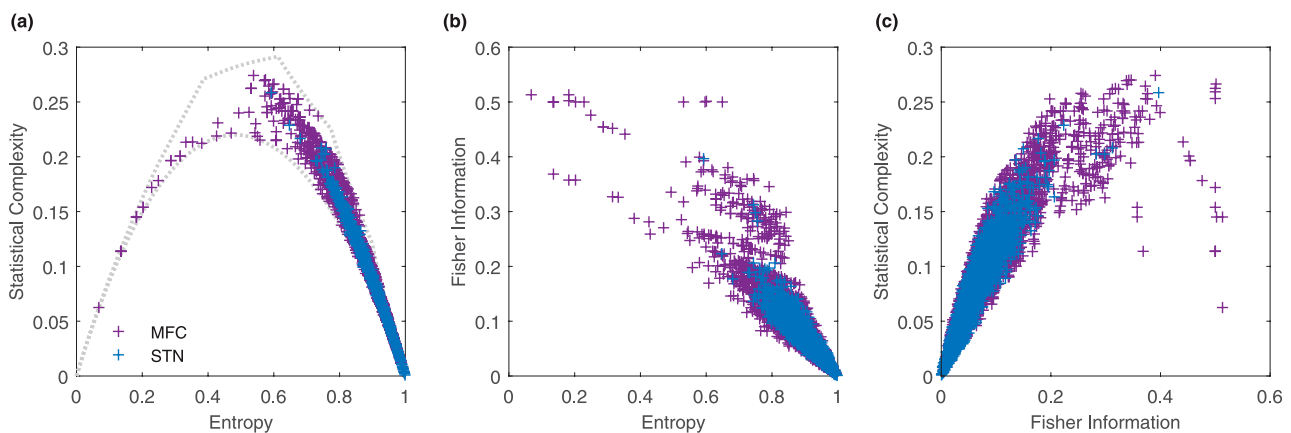


FIG. 10. Comparison of dynamics in the subthalamic nucleus (STN) and the medial frontal cortex (MFC) using $D = 3$. Shannon entropy, statistical complexity, and Fisher information calculated on local field potentials (LFPs) using an embedding dimension of Bandt and Pompe $D = 3$ and a temporal window of 200 ms. Blue represents data from the STN and violet represents data from the MFC. (a) Complexity–entropy causality plane. (b) Shannon entropy–Fisher information plane. (c) Statistical complexity–Fisher information plane.

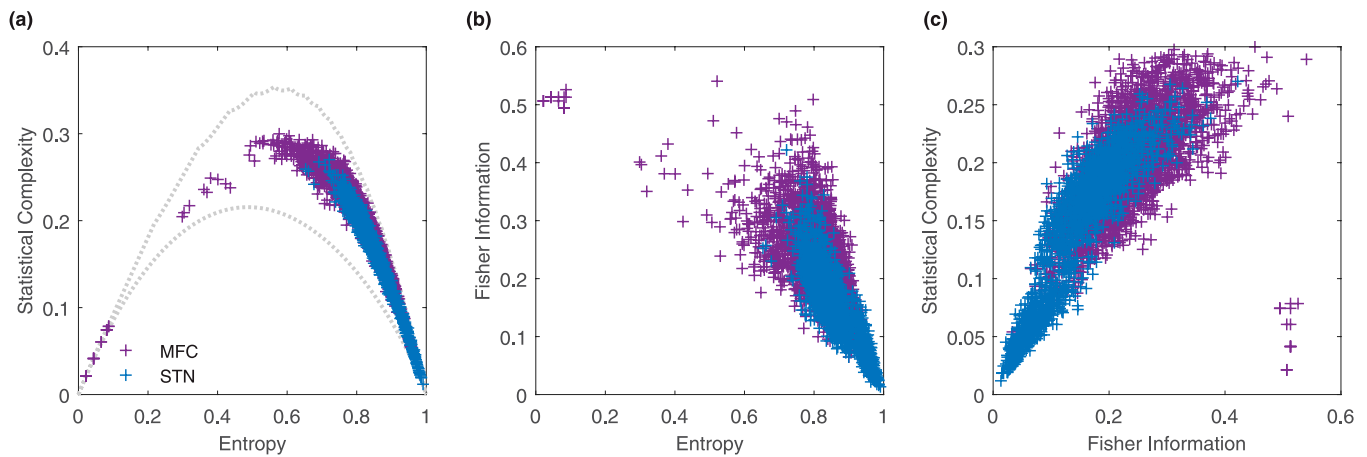


FIG. 11. Same as Fig. 10, but with a BP dimension $D = 4$ and a temporal window of 400 ms.

is a zoomed-in version of Fig. 4 on the region between 1.5×10^5 and 2.0×10^5 ms, the same information is shown. In all cases, the Hénon map presents a higher density of positive Lyapunov exponents, indicating its predominantly chaotic behavior. In Figs. 4 and 5, a higher number of positive exponents can be observed for the Hénon map. In Fig. 4(b), more negative exponents can be seen for the STN, and in Fig. 4(c), a higher number of negative exponents is found for the MFC. Contrary to what would be expected, the Lyapunov exponents suggest a less chaotic behavior in the healthy region. In Fig. 6, it can be observed that the Hénon map continues to have a higher density of positive Lyapunov exponents, indicating a predominantly chaotic behavior. However, all systems show an

increase in positive exponents when the time window is increased to 400 ms, with this change being more noticeable in Figs. 6(b) and 6(c), which show the experimental data. Upon closer examination in Fig. 7, the differences in chaos between the systems become less noticeable. In Figs. 8(a) and 9(a), the complexity–entropy causality plane can be seen. It can be observed that for a temporal window of 200 ms, the Hénon map approximates the dynamics of the STN LFPs are quite well if we consider that the different noise components are located in the bottom right corner. This same behavior is reflected in Figs. 8(b) and 9(b), as well as in Figs. 8(c) and 9(c), where overlapping behaviors are seen within the Fisher information–entropy and complexity–Fisher information planes.

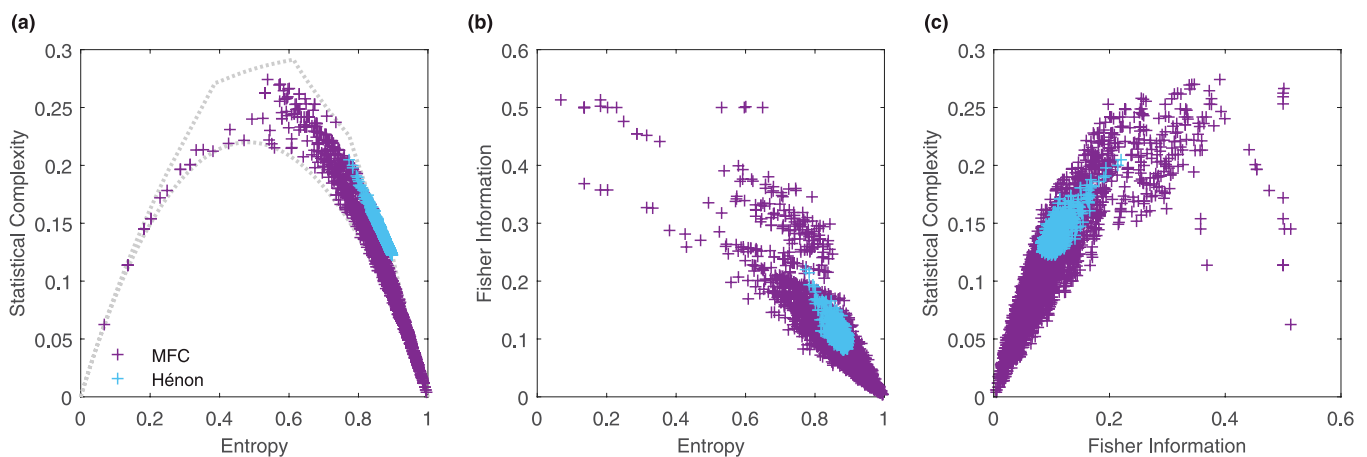


FIG. 12. Comparison of dynamics in the medial frontal cortex (MFC) and the Hénon map using $D = 3$. Shannon entropy, statistical complexity, and Fisher information calculated on local field potentials (LFPs) using an embedding dimension of Bandt and Pompe $D = 3$ and a time window of 200 ms. Violet represents data from the MFC and light blue represents data from the Hénon map. (a) Complexity–entropy causality plane. (b) Shannon entropy–Fisher information plane. (c) Statistical complexity–Fisher information plane.

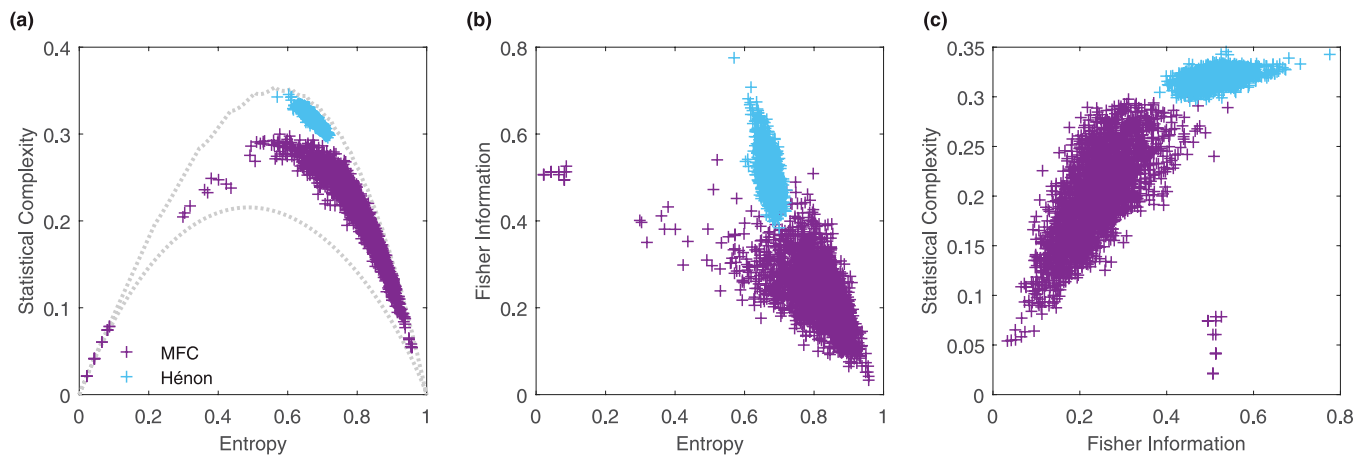


FIG. 13. Same as Fig. 12, but with a BP dimension $D = 4$ and a time window of 400 ms.

However, when the temporal window is increased to 400 ms in order to implement the embedded dimension $D = 4$, the dynamic behaviors separate. In Fig. 9(a), it can be seen that the Hénon map migrates toward the chaotic region separating from the STN LFPs. This separation is also evident in Figs. 9(b) and 9(c).

In Figs. 11 and 10, the dynamics of local field potentials (LFPs) from the subthalamic nucleus (STN) of Parkinson's disease patients are compared to the dynamics of the medial frontal cortex (MFC) region, which is assumed to have similar neural activity but from healthy subjects. In Fig. 11, BP dimension $D = 4$ and a temporal

window of 400 ms are used, while in Fig. 10, BP dimension $D = 3$ and a temporal window of 200 ms are used. In both figures, it is apparent that the data from the healthy MFC region exhibit more chaotic components and several points shift into the region of regular oscillations in the complexity–entropy causality plane [Figs. 11(a) and 10(a)]. It should be noted that in $D = 4$ (Fig. 11), the density of points in the regular oscillation region is higher than in $D = 3$ (Fig. 10). This indicates that the analyzed data have partially similar dynamic behavior, as they overlap in many points, but the LFP from the MFC region (with normal,

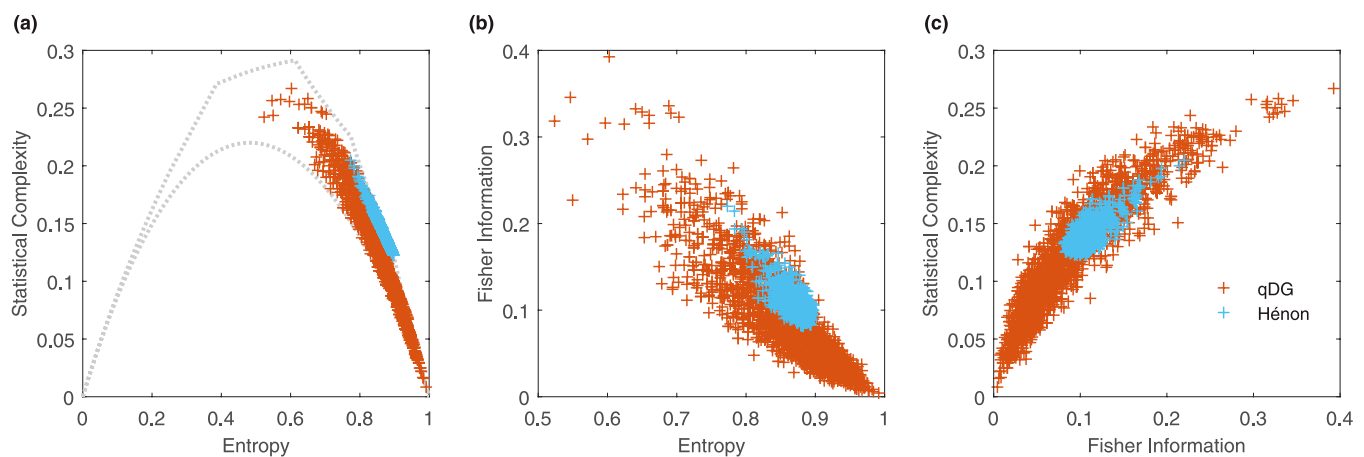


FIG. 14. Comparison of dynamics in the Hénon map and a dichotomized q -Gaussian model using $D = 3$. Shannon entropy, statistical complexity, and Fisher information calculated on local field potentials (LFPs) using an embedding dimension of Bandt and Pompe $D = 3$ and a time window of 200 ms. Light blue represents data from the Hénon map and orange represents data from the dichotomized q -Gaussian model. (a) Complexity–entropy causality plane. (b) Shannon entropy–Fisher information plane. (c) Statistical complexity–Fisher information plane.

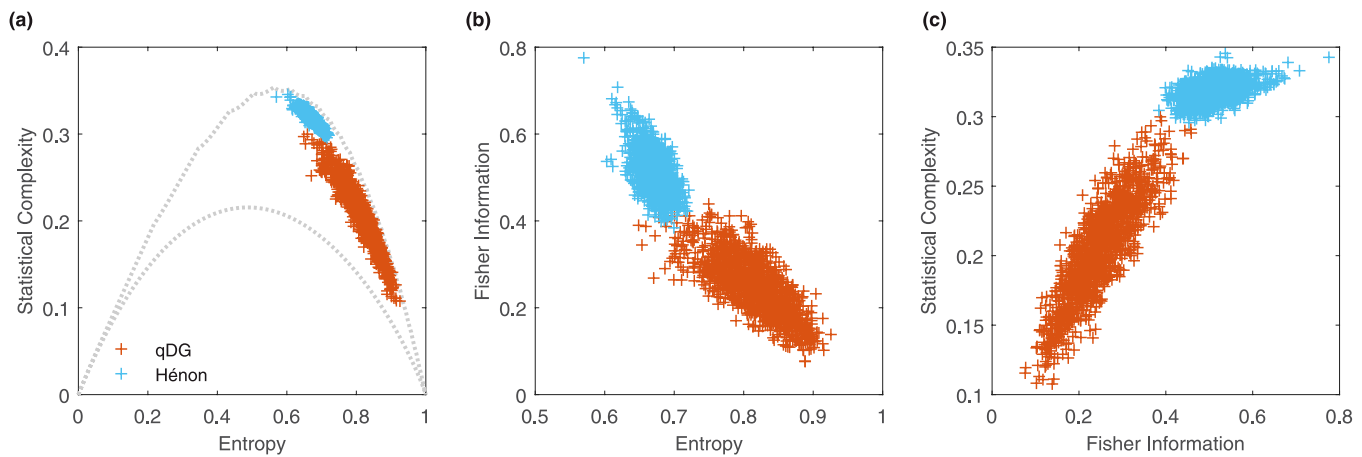


FIG. 15. Same as Fig. 14, but with a BP dimension $D = 4$ and a 400 ms time window.

non-pathological activity) shows more chaotic and regular oscillation characteristics. These overlaps and differences can also be seen in the Shannon entropy–Fisher information plane [Figs. 11(b) and 10(b)] and the statistical complexity–Fisher information plane [Figs. 11(c) and 10(c)].

In the case of the comparison of the MFC LFP data and the Hénon map, the greater variety of behaviors displayed by the neurophysiological data is evident in all figures. In Fig. 12 with BP dimension $D = 3$, in the complexity–entropy causality plane [Fig. 12(a)], the MFC data almost cover the entire spectrum of the plane, passing through the noise region, approaching chaotic characteristics, and reaching the region of regular oscillations. Meanwhile, the Hénon map is positioned in a confined region. In the case of $D = 4$ [Fig. 13(a)], the experimental data values open up even more toward regular oscillations, while Hénon is compressed and positioned in the upper region of the causality plane in the chaotic region. Continuing the description of figures, in Figs. 14 and 15, the dynamics of the Hénon map are compared. In Fig. 14, BP dimension $D = 3$ and a temporal window of 200 ms are used, while in Fig. 15, BP dimension $D = 4$ and a temporal window of 400 ms are used. It can be noted that the dynamic behavior found in these figures, where the q -DG model is shown alongside the Hénon map, is analogous to the behavior found in the figures comparing the dynamics between the Hénon map and the STN LFPs. This is observed in both the similarities in $D = 3$ and the differences seen in $D = 4$. The behavior of the q -DG is similar to that of the STN LFPs.

It should be noted that the comparisons between the models and experimental data have been visualized qualitatively through the figures of the calculated results. This is primarily because some of the data appear distinctly separated in the images, while other results exhibit partial overlap. The partial overlaps were considered from the analysis of the marginal distributions, as shown in Appendix A for the case of $D = 3$. Appendix A presents the marginal distributions for the complexity–entropy causality plane (Fig. 16), Shannon entropy–Fisher information plane (Fig. 17), and statistical

complexity–Fisher information plane (Fig. 18) for the $D = 3$ case. The figures show how the results of each model are distributed in each plane, allowing the degree of overlap between them to be evaluated. The MFC is represented in violet, the STN in blue, the q -DG model in orange, and the Hénon map in light blue. The figures provide a more detailed analysis of the overlaps observed in the calculated results.

The dynamic behavior of these systems is highly dependent on the temporal scale studied, with the dynamics of the Hénon map becoming increasingly different from those of biological and artificial neural systems as the size of the sample studied increases. This can be seen in the comparison of the Hénon map with the STN LFPs and the q -DG model, where the Hénon map exhibits more chaotic and less regular oscillation characteristics in the causality plane compared to the neurophysiological and artificial data. This trend is also observed in the Lyapunov exponent figures, where the Hénon map exhibits more chaotic behavior as the temporal window increases. This suggests that the Hénon map may not accurately represent the complex dynamic behaviors observed in real-world biological systems, particularly at larger temporal scales. In conclusion, the complexity–entropy causality plane was found to be a useful tool for comparing the dynamics of different systems. By calculating the Shannon entropy and statistical complexity of the time series and plotting them on a two-dimensional plane, it was possible to see if the dynamics of similar time series exhibited similarities or differences in terms of entropy and complexity.

The results of this study showed that the Hénon map was able to approximate some characteristics of the dynamics of the STN LFPs when considering a temporal window of 200 ms and an embedding dimension of $D = 3$. However, when the temporal window was increased to 400 ms and the embedding dimension was increased to $D = 4$, the dynamic behaviors separated, with the Hénon map shifting toward the chaotic region and away from the STN LFPs.

The q -DG model was also found to be able to imitate the dynamics of the STN LFPs, with a higher overlap in the complexity–entropy causality plane when considering a temporal window of 200 ms and an embedding dimension of $D = 3$. However, the q -DG model showed less overlap with the MFC LFPs (due to the fact that it does not have regular oscillation components), indicating that it may not be as effective at reproducing the dynamics of healthy brain regions.

It is worth noting that neurophysiological recordings of LFPs often have large noise components due to the measurement methodologies, and it is not certain that experimental data in the noise region of the complexity–entropy plane do not largely originate from the noise introduced by the reading method.

Overall, the Hénon map barely reproduced a part of the full spectrum of STN LFP dynamics, with the greatest overlap observed when considering a temporal window of 200 ms and an embedding dimension of $D = 3$. However, further research is needed to determine if the Hénon map can be implemented as a therapeutic tool for stimulating patients with Parkinson's disease. The q -DG model also showed potential as a tool for imitating brain dynamics (although its chaotic components are smaller and it does not have regular oscillation components).

The results suggest that normal neural dynamics in the STN region have a more complex spectrum within the complexity–entropy causality plane that cannot be solely represented by chaotic models. It is important to consider the temporal scale at which the Hénon map could be applied, as it is constrained by the required sampling frequency. It should also be noted that most of the similarities were observed for small temporal dimensions and signals from pathological activity. It would be interesting to study whether normal neural activity in the STN region exhibits regular oscillations, as the presence of these components would further distance the Hénon map from the neural activity in this region, rendering it even less suitable for modeling the activity of the STN.

The reader should consider the sizes of the analyzed windows and embedding dimensions, as two factors affect the separation of results. Increasing the embedding dimension (D) accounts for more causal information from the signals, while increasing the window size enhances the precision of the calculated information-theoretic quantifiers. [Appendix B](#) demonstrates the effect of window size on the calculation of the quantifiers for the analyzed data. However, it is important to note that increasing the temporal windows over experimental data may result in a possible loss of timing precision, as highlighted by Panzeri *et al.*⁵⁷ It is crucial to interpret these results while considering the trade-off between the increased amount of information encoded in neurophysiological records using small windows (see Refs. 57–59 for techniques on how to maximize this information) and the loss of statistical significance resulting from the application of information-theoretic quantifiers themselves when analyzing short time series.

V. CONCLUSIONS

In summary, both the Hénon map and q -DG model showed some ability to reproduce certain features of the LFP dynamics

analyzed in this study, although care must be taken in choosing appropriate parameters, sampling rates, and temporal scales. However, neither model was able to completely imitate the dynamics of the LFPs. The Hénon map was able to approximate some characteristics of the STN LFP dynamics when considering a temporal window of 200 ms and an embedding dimension of $D = 3$, but when the temporal window was increased to 400 ms and the embedding dimension was increased to $D = 4$, the dynamic behaviors separated, with the Hénon map shifting toward the chaotic region and away from the STN LFPs. The q -DG model showed a greater overlap with the STN LFPs when considering a temporal window of 200 ms and an embedding dimension of $D = 3$, but it did not have regular oscillation components and, therefore, did not show as much overlap with the MFC LFPs. It is important to consider the noise present in neurophysiological recordings of LFPs and the potential impact on the complexity–entropy plane, as well as the trade-off that exists regarding the possible loss of information associated with increasing the window size and the precision of calculations by the information-theoretic quantifiers. Further research is needed to determine the suitability of the Hénon map as a therapeutic tool for stimulating patients with Parkinson's disease, as well as to study the presence of regular oscillations in normal neural activity in the STN region.

ACKNOWLEDGMENTS

We are grateful for the funding provided by IFLP-CONICET Argentina (No. PUE 22920170100066CO) and Universidad Nacional de La Plata, Argentina (Project No. 80120190100127LP).

AUTHOR DECLARATIONS

Conflict of Interest

The authors have no conflicts to disclose.

Author Contributions

Natalí Guisande: Conceptualization (equal); Data curation (equal); Formal analysis (equal); Investigation (equal); Methodology (equal); Software (equal); Validation (equal); Visualization (equal); Writing – original draft (equal); Writing – review & editing (equal). **Montserrat Pallares di Nunzio:** Conceptualization (equal); Data curation (equal); Formal analysis (equal); Investigation (equal); Methodology (equal); Validation (equal). **Nataniel Martínez:** Conceptualization (equal); Data curation (equal); Investigation (equal). **Oswaldo A. Rosso:** Conceptualization (equal); Data curation (equal); Formal analysis (equal); Funding acquisition (equal); Investigation (equal); Methodology (equal); Project administration (equal); Resources (equal); Software (equal); Supervision (equal); Validation (equal); Visualization (equal); Writing – original draft (equal); Writing – review & editing (equal). **Fernando Montani:** Conceptualization (equal); Data curation (equal); Formal analysis (equal); Funding acquisition (equal); Investigation (equal); Methodology (equal); Project administration (equal); Resources (equal); Software (equal); Supervision (equal); Validation (equal); Visualization (equal); Writing – original draft (equal); Writing – review & editing (equal).

DATA AVAILABILITY

Experimental data used in this study were obtained from two sources. The first is the University of Oxford database at <https://data.mrc.ox.ac.uk/data-set/human-lfp-recordings-stn-during-sequential-conflict-task>, Refs. 11 and 53. The second source of data is the Montreal Neurological Institute (MNI) Open iEEG Atlas at <https://mni-open-ieegatlas.research.mcgill.ca/>, Refs. 54–56. This collaborative project, involving the Montreal Neurological Institute and Hospital, the Grenoble-Alpes University Hospital, and the Centre hospitalier de l'Université de Montréal, provides open access to a collection of normal intracranial EEG activity.

APPENDIX A: MARGINAL DISTRIBUTIONS OF THE COMPLEXITY-ENTROPY CAUSALITY PLANE FOR $D = 3$.

The marginal distributions of the complexity-entropy causality plane for MFC, STN, q -DG, and Hénon are shown in Fig. 16. The components are represented by different colors: violet for MFC, blue for STN, orange for q -DG, and light blue for Hénon. The same information for the Shannon entropy-Fisher information and Fisher information-statistical complexity planes is shown in Figs. 17 and 18, respectively.

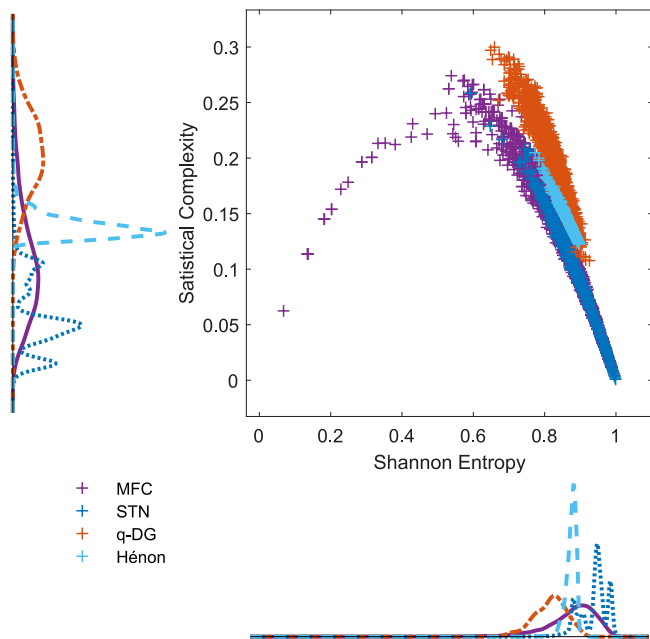


FIG. 16. Marginal distributions on the complexity-entropy causality plane for $D = 3$. The medial frontal cortex (MFC) is represented in violet, the subthalamic nucleus (STN) in blue, the q -DG model in orange, and the Hénon map in light blue.

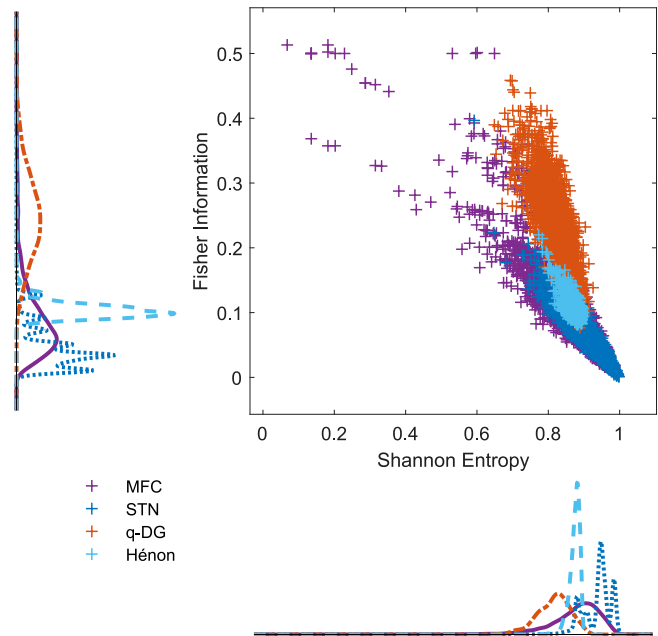


FIG. 17. Marginal distributions on the Shannon entropy-Fisher information plane for $D = 3$. The medial frontal cortex (MFC) is represented in violet, the subthalamic nucleus (STN) in blue, the q -DG model in orange, and the Hénon map in light blue.

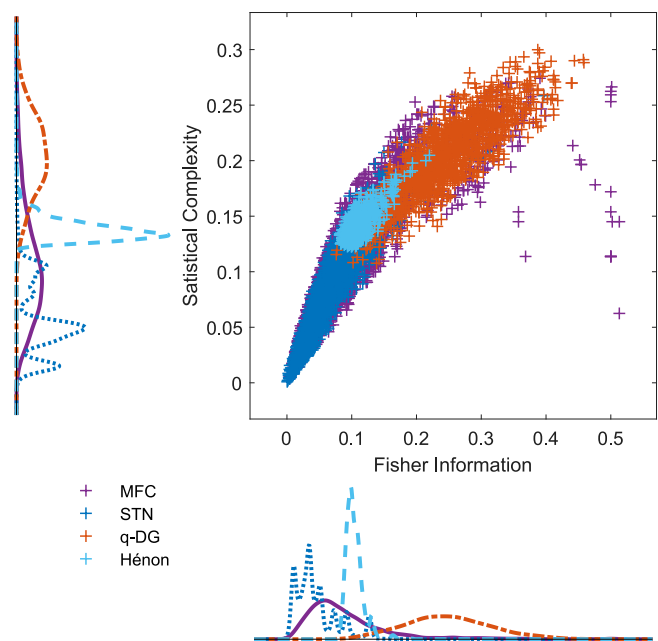


FIG. 18. Marginal distributions on the statistical complexity-Fisher information for $D = 3$. The medial frontal cortex (MFC) is represented in violet, the subthalamic nucleus (STN) in blue, the q -DG model in orange, and the Hénon map in light blue.

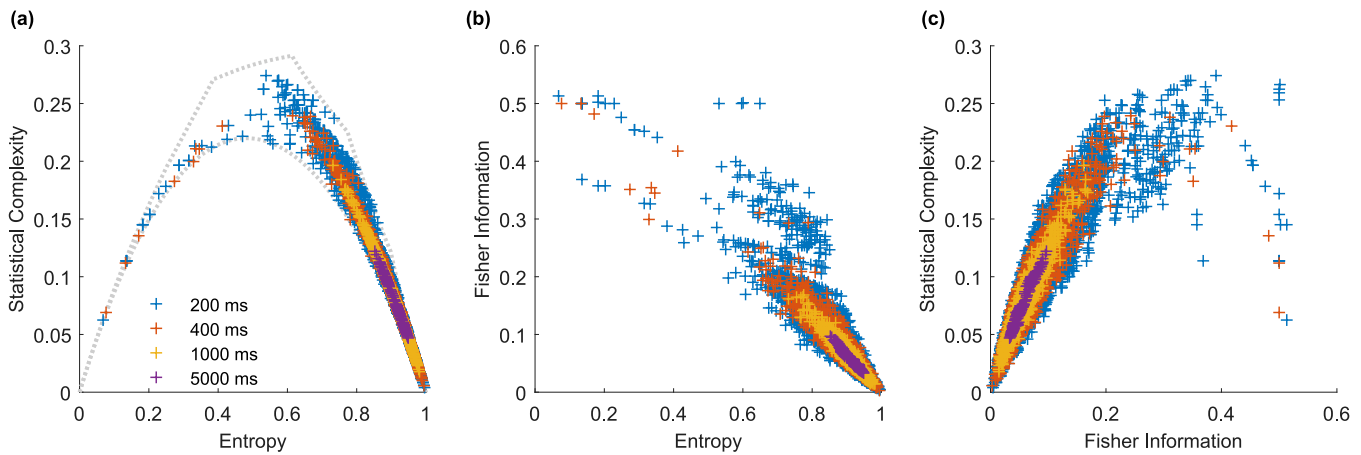


FIG. 19. Effect of window size on information-theoretic quantifiers in MFC using $D = 3$. Shannon entropy, statistical complexity, and Fisher information calculated on local field potentials (LFPs) using an embedding dimension of Bandt and Pompe $D = 3$. The figure shows a comparison of these quantifiers for four different time windows in MFC, with each figure [(a)–(c)] representing the comparison of all window sizes. The colors used to represent the different window sizes are as follows: light blue (200 ms), orange (400 ms), yellow (1000 ms), and violet (5000 ms). (a) shows the complexity–entropy causality plane. (b) shows the Shannon entropy–Fisher information plane. (c) shows the statistical complexity–Fisher information plane.

APPENDIX B: EFFECT OF WINDOW SIZE ON IMPLEMENTATION OF INFORMATION-THEORETIC QUANTIFIERS

This section presents some examples of how the precision of the information-theoretic quantifiers used is affected by the window size used for PDF calculation. Only MFC experimental data results are presented since their longer time series allows for analysis at $D = 3$ (Fig. 19) and $D = 4$ (Fig. 20). Theoretical models are

presented for both $D = 3$ and $D = 4$, as the length of the time series is not limited. Figures 21 and 22 correspond to the Hénon map, while Figs. 23 and 24 correspond to the q -DG model. It is worth noting that, as the temporal window size increases, the point cloud dispersion of all the quantifiers becomes compressed into more restricted regions, increasing their precision. This effect is observed in all the analyzed data and dimensions. A comprehensive analysis of this topic is outside the scope of this work.

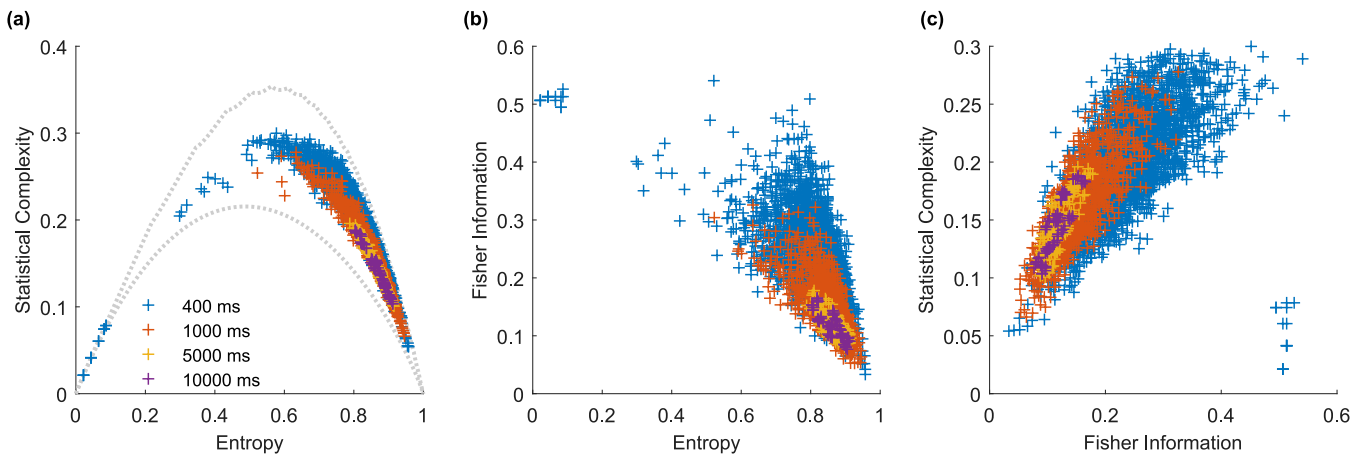


FIG. 20. Effect of window size on information-theoretic quantifiers in MFC using $D = 3$. Shannon entropy, statistical complexity, and Fisher information calculated on local field potentials (LFPs) using an embedding dimension of Bandt and Pompe $D = 4$. The figure shows a comparison of these quantifiers for four different time windows in MFC, with each figure [(a)–(c)] representing the comparison of all window sizes. The colors used to represent the different window sizes are as follows: light blue (400 ms), orange (1000 ms), yellow (5000 ms), and violet (10 000 ms). (a) shows the complexity–entropy causality plane. (b) shows the Shannon entropy–Fisher information plane. (c) shows the statistical complexity–Fisher information plane.

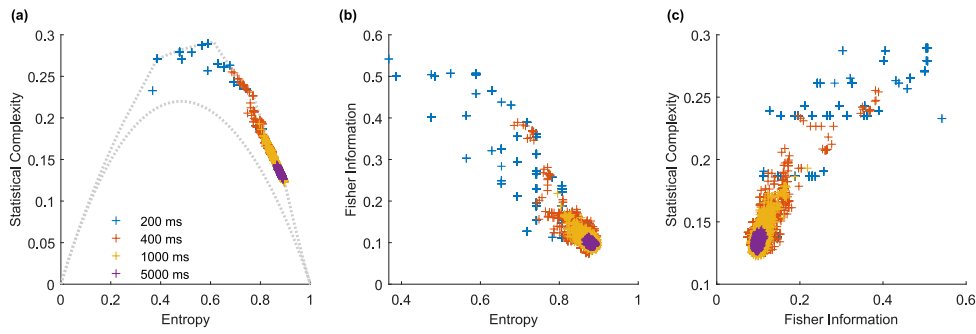


FIG. 21. Effect of window size on information-theoretic quantifiers in the Hénon map using $D = 3$. Shannon entropy, statistical complexity, and Fisher information calculated on time series generated with the Hénon map, using an embedding dimension of Bandt and Pompe $D = 3$. The figure shows a comparison of these quantifiers for four different time windows, with each figure [(a)–(c)] representing the comparison of all window sizes. The colors used to represent the different window sizes are as follows: light blue (200 ms), orange (400 ms), yellow (1000 ms), and violet (5000 ms). (a) shows the complexity–entropy causality plane. (b) shows the Shannon entropy–Fisher information plane. (c) shows the statistical complexity–Fisher information plane. The results are an average of the results of time series generated with the two components of the map.

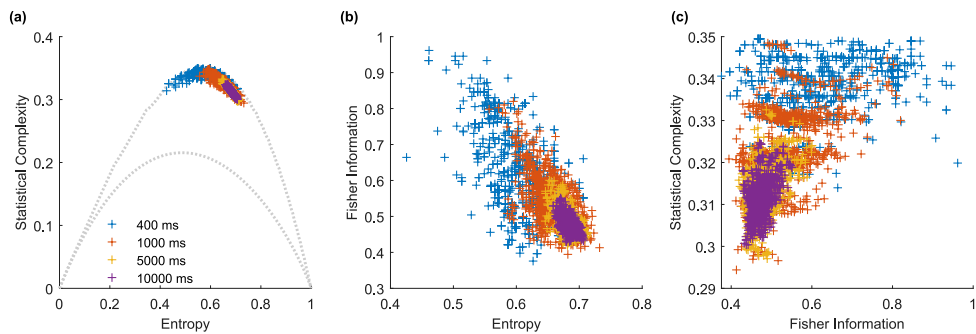


FIG. 22. Effect of window size on information-theoretic quantifiers in the Hénon map using $D = 4$. Shannon entropy, statistical complexity, and Fisher information calculated on time series generated with the Hénon map, using an embedding dimension of Bandt and Pompe $D = 3$. The figure shows a comparison of these quantifiers for four different time windows, with each figure [(a)–(c)] representing the comparison of all window sizes. The colors used to represent the different window sizes are as follows: light blue (400 ms), orange (1000 ms), yellow (5000 ms), and violet (10 000 ms). (a) shows the complexity–entropy causality plane. (b) shows the Shannon entropy–Fisher information Plane. (c) shows the statistical complexity–Fisher information plane. The results are an average of the results of time series generated with the two components of the map.

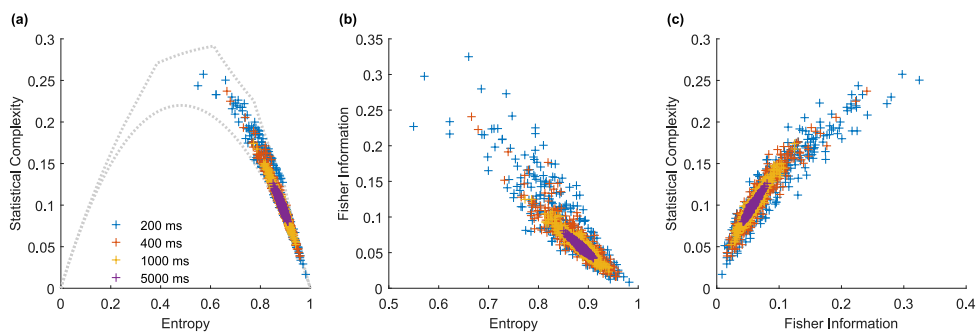


FIG. 23. Effect of window size on information-theoretic quantifiers in the q -DG model using $D = 3$. Shannon entropy, statistical complexity, and Fisher information calculated on the sum of spike trains generated by the q -DG model, using an embedding dimension of Bandt and Pompe $D = 3$. The figure shows a comparison of these quantifiers for four different time windows, with each figure [(a)–(c)] representing the comparison of all window sizes. The colors used to represent the different window sizes are as follows: light blue (200 ms), orange (400 ms), yellow (1000 ms), and violet (5000 ms). (a) shows the complexity–entropy causality plane. (b) shows the Shannon entropy–Fisher information plane. (c) shows the statistical complexity–Fisher information plane. The orange color represents the q -DG model, which is a dichotomized Gaussian model.

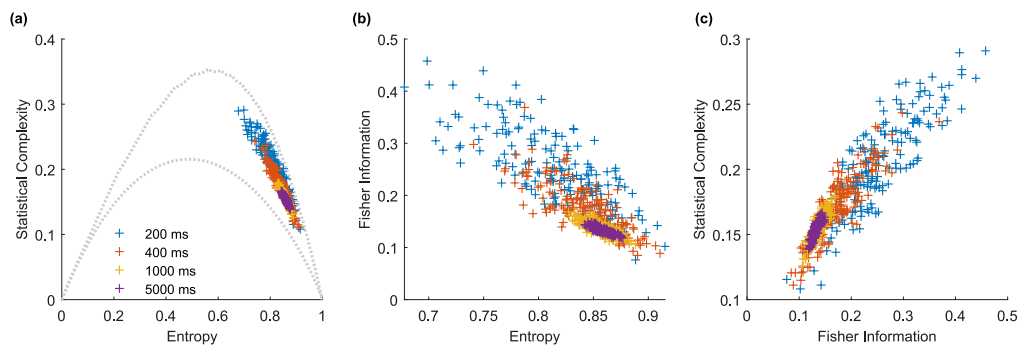


FIG. 24. Effect of window size on information-theoretic quantifiers in the q -DG model using $D = 4$. Shannon entropy, statistical complexity, and Fisher information calculated on the sum of spike trains generated by the q -DG model, using an embedding dimension of Bandt and Pompe $D = 3$. The figure shows a comparison of these quantifiers for four different time windows, with each figure [(a)–(c)] representing the comparison of all window sizes. The colors used to represent the different window sizes are as follows: light blue (400 ms), orange (1000 ms), yellow (5000 ms), and violet (10 000 ms). (a) shows the complexity–entropy causality plane. (b) shows the Shannon entropy–Fisher information plane. (c) shows the statistical complexity–Fisher information plane. The orange color represents the q -DG model, which is a dichotomized Gaussian model.

REFERENCES

- L. Pezard and J.-L. Nandrino, “Dynamical paradigm in psychopathology: ‘Chaos theory,’ from physics to psychiatry,” *L’Encéphale* **27**, 260–268 (2001), available at <http://hdl.handle.net/20.500.12210/39357>.
- L. Zhang, “Design and implementation of neural network based chaotic system model for the dynamical control of brain stimulation” (2017).
- A. L. Goldberger, “Fractal variability versus pathologic periodicity: Complexity loss and stereotypy in disease,” *Perspect. Biol. Med.* **40**, 543–561 (1997).
- M. C. Mackey and L. Glass, “Oscillation and chaos in physiological control systems,” *Science* **197**, 287–289 (1977).
- M. C. Mackey and J. G. Milton, “Dynamical diseases,” *Ann. N.Y. Acad. Sci.* **504**, 16–32 (1987).
- E. Pereda, R. Q. Quiroga, and J. Bhattacharya, “Nonlinear multivariate analysis of neurophysiological signals,” *Prog. Neurobiol.* **77**, 1–37 (2005).
- R. Falahian, M. M. Dastjerdi, M. Molaie, S. Jafari, and S. Gharibzadeh, “Artificial neural network-based modeling of brain response to flicker light,” *Nonlinear Dyn.* **81**, 1951–1967 (2015).
- H. Korn and P. Faure, “Is there chaos in the brain? II. Experimental evidence and related models,” *C. R. Biol.* **326**, 787–840 (2003).
- L. Zhang, “Hénon map chaotic system critical points analysis and classification for the dynamic control of brain stimulation,” in *2017 IEEE XXIV International Conference on Electronics, Electrical Engineering and Computing (INTERCON)* (IEEE, 2017), pp. 1–4.
- L. Zhang, “Hénon map chaotic system analysis and vhdl-based fixed-point fpga implementation for brain stimulation,” in *2017 IEEE 30th Canadian Conference on Electrical and Computer Engineering CCECE* (IEEE, 2017).
- Z. E. Patai, T. Foltynie, P. Limousin, H. Akram, L. Zrinzo, R. Bogacz, and V. Litvak, “Conflict detection in a sequential decision task is associated with increased cortico-subthalamic coherence and prolonged subthalamic oscillatory response in the beta band,” *bioRxiv* (2022), see <https://www.biorxiv.org/content/early/2022/02/10/2020.06.09.141713.full.pdf>.
- M. Frank, “Hold your horses: A dynamic computational role for the subthalamic nucleus in decision making,” *Neural Netw.* **19**, 1120–36 (2006).
- Y. M. Vachez and M. C. Creed, “Deep brain stimulation of the subthalamic nucleus modulates reward-related behavior: A systematic review,” *Front. Hum. Neurosci.* **14**, 578564 (2020).
- B. Seymour, M. Barbe, P. Dayan, T. Shiner, R. Dolan, and G. Fink, “Deep brain stimulation of the subthalamic nucleus modulates sensitivity to decision outcome value in Parkinson’s disease,” *Sci. Rep.* **6**, 32509 (2016).
- M. C. Biagioni, K. Sharma, H. A. Migdadi, and A. Cucca, “Non-invasive neuromodulation therapies for Parkinson’s disease,” in *Parkinson’s Disease—Understanding Pathophysiology and Developing Therapeutic Strategies* (InTech, 2018).
- K.-H. S. Chen and R. Chen, “Invasive and noninvasive brain stimulation in Parkinson’s disease: Clinical effects and future perspectives,” *Clin. Pharmacol. Ther.* **106**, 763–775 (2019).
- Y. Scharf, “A chaotic outlook on biological systems,” *Chaos, Solitons Fractals* **95**, 42–47 (2017).
- W. Xingyuan and L. Chao, “Researches on chaos phenomenon of EEG dynamics model,” *Appl. Math. Comput.* **183**, 30–41 (2006).
- J. Humplik and G. Tkačik, “Probabilistic models for neural populations that naturally capture global coupling and criticality,” *PLoS Comput. Biol.* **13**, e1005763 (2017).
- M. Hénon, “A two-dimensional mapping with a strange attractor,” *Commun. Math. Phys.* **50**, 69–77 (1976).
- C. Bandt and B. Pompe, “Permutation entropy: A natural complexity measure for time series,” *Phys. Rev. Lett.* **88**, 174102 (2002).
- S.-I. Amari, H. Nakahara, S. Wu, and Y. Sakai, “Synchronous firing and higher-order interactions in neuron pool,” *Neural Comput.* **15**, 127–142 (2003).
- J. H. Macke, M. Opper, and M. Bethge, “The effect of pairwise neural correlations on global population statistics,” Max-Planck Institute for Biological Cybernetics, Technical Report No. 183 (2009).
- J. H. Macke, M. Opper, and M. Bethge, “An analytically tractable model of neural population activity in the presence of common input explains higher-order correlations and entropy,” [http://arxiv.org/abs/arXiv:1009.2855v2\(g-bio.nc\)](http://arxiv.org/abs/arXiv:1009.2855v2(g-bio.nc)) (2010).
- J. H. Macke, P. Berens, A. S. Ecker, A. S. Tolias, and M. Bethge, “Generating spike trains with specified correlation coefficients,” *Neural Comput.* **21**, 397–423 (2009).
- L. Montangie and F. Montani, “Higher-order correlations in common input shapes the output spiking activity of a neural population,” *Physica A* **471**, 845–861 (2017).
- L. Montangie, “Modelos minimales y teoría de la información de poblaciones neuronales,” Ph.D. thesis (Universidad Nacional de La Plata, 2017).
- O. Rosso and C. Masoller, “Detecting and quantifying temporal correlations in stochastic resonance via information theory measures,” *Eur. Phys. J. B* **69**, 37–43 (2009).
- F. Montani and O. A. Rosso, “Entropy-complexity characterization of brain development in chickens,” *Entropy* **16**, 4677–4692 (2014).
- O. Rosso and C. Masoller, “Detecting and quantifying stochastic and coherence resonances via information-theory complexity measurements,” *Phys. Rev. E* **79**, 040106(R) (2009).

- ³¹K. Keller and H. Lauffer, "Symbolic analysis of high-dimensional time series," *Int. J. Bifurcat. Chaos* **13**, 2657–2668 (2003).
- ³²A. A. B. Pessa and H. V. Ribeiro, "Ordpy: A Python package for data analysis with permutation entropy and ordinal network methods," *Chaos* **31**, 063110 (2021).
- ³³D. Feldman and J. Crutchfield, "Measures of statistical complexity: Why?," *Phys. Lett. A* **238**, 244–252 (1998).
- ³⁴C. Shannon and W. Weaver, *The Mathematical Theory of Communication* (University of Illinois Press, Champaign, IL, 1949), ISBN-10: 0252725484.
- ³⁵M. Martín, A. Plastino, and O. Rosso, "Generalized statistical complexity measures: Geometrical and analytical properties," *Physica A* **369**, 439–462 (2006).
- ³⁶R. López-Ruiz, H. Mancini, and X. Calbet, "A statistical measure of complexity," *Phys. Lett. A* **209**, 321–326 (1995).
- ³⁷P. Lamberti, M. Martín, A. Plastino, and O. Rosso, "Intensive entropic non-triviality measure," *Physica A* **334**, 119–131 (2008).
- ³⁸I. Grosse, P. Bernaola-Galván, P. Carpena, R. Román-Roldán, J. Oliver, and H. Stanley, "Analysis of symbolic sequences using the Jensen-Shannon divergence," *Phys. Rev. E* **65**, 041905 (2002).
- ³⁹D. Feldman, C. McTague, and J. Crutchfield, "The organization of intrinsic computation: Complexity-entropy diagrams and the diversity of natural information processing," *Chaos* **18**, 043106 (2008).
- ⁴⁰R. Fisher, "On the mathematical foundations of theoretical statistics," *Philos. Trans. R. Soc. London, Ser. A* **222**, 309–368 (1922).
- ⁴¹B. Frieden, *Science from Fisher Information: A Unification* (Cambridge University Press, Cambridge, 2004).
- ⁴²A. Mayer, C. Pawłowski, and H. Cabezas, "Fisher information and dynamic regime changes in ecological systems," *Ecol. Modell.* **195**, 72–82 (2006).
- ⁴³O. Rosso, L. De Micco, A. Plastino, and H. Larrondo, "Info-quantifiers' map-characterization revisited," *Physica A* **389**, 249–262 (2010).
- ⁴⁴F. Olivares, A. Plastino, and O. Rosso, "Ambiguities in the Bandt-Pompe's methodology for local entropic quantifiers," *Physica A* **391**, 2518–2526 (2012).
- ⁴⁵F. Olivares, A. Plastino, and O. Rosso, "Contrasting chaos with noise via local versus global information quantifiers," *Phys. Lett. A* **376**, 1577–1583 (2012).
- ⁴⁶K. Zografos, K. Ferentinos, and T. Papaioannou, "Discrete approximations to the Csiszár, Rényi, and Fisher measures of information," *Can. J. Stat.* **14**, 355–366 (1986).
- ⁴⁷L. Pardo, D. Morales, K. Ferentinos, and K. Zografos, "Discretization problems on generalized entropies and R-divergences," *Kybernetika* **30**, 445–460 (1994).
- ⁴⁸M. Madiman, O. Johnson, and I. Kontoyiannis, "Fisher information, compound Poisson approximation, and the Poisson channel," in *IEEE International Symposium on Information Theory, ISIT* (IEEE, Nice, 2007), pp. 976–980.
- ⁴⁹P. Sanchez-Moreno, J. Dehesa, and R. Yanez, "Discrete densities and Fisher information," in *Proceedings of the 14th International Conference on Difference Equations and Applications* (Üğür-Bahçeşehir University Publishing Company, Istanbul, 2009), pp. 291–298.
- ⁵⁰F. Pennini and A. Plastino, "Reciprocity relations between ordinary temperature and the Frieden-Soffer Fisher temperature," *Phys. Rev. E* **71**, 047102 (2005).
- ⁵¹M. Zanin and F. Olivares, "Ordinal patterns-based methodologies for distinguishing chaos from noise in discrete time series," *Commun. Phys.* **4**, 190 (2021).
- ⁵²O. Rosso, H. Larrondo, M. Martín, A. Plastino, and M. Fuentes, "Distinguishing noise from chaos," *Phys. Rev. Lett.* **99**, 154102 (2007).
- ⁵³R. Bogacz, V. Litvak, A. Oswal, S. Little, D. Pedrosa, D. Herz, V. Dayal, and E. Zita Patai, "Human LFP recordings from STN during sequential conflict task," University of Oxford, <https://data.mrc.ox.ac.uk/data-set/human-lfp-recordings-stn-during-sequential-conflict-task> (2020).
- ⁵⁴B. Frauscher, N. von Ellenrieder, R. Zelmann, I. Doležalová, L. Minotti, A. Olivier, J. Hall, D. Hoffmann, D. K. Nguyen, P. Kahane, F. Dubeau, and J. Gotman, "Atlas of the normal intracranial electroencephalogram: Neurophysiological awake activity in different cortical areas," *Brain* **141**, 1130–1144 (2018).
- ⁵⁵B. Frauscher, N. von Ellenrieder, R. Zelmann, C. Rogers, D. K. Nguyen, P. Kahane, F. Dubeau, and J. Gotman, "High-frequency oscillations in the normal human brain," *Ann. Neurol.* **84**, 374–385 (2018).
- ⁵⁶N. von Ellenrieder, J. Gotman, R. Zelmann, C. Rogers, D. K. Nguyen, P. Kahane, F. Dubeau, and B. Frauscher, "How the human brain sleeps: Direct cortical recordings of normal brain activity," *Ann. Neurol.* **87**, 289–301 (2020).
- ⁵⁷S. Panzeri, R. S. Petersen, S. R. Schultz, M. Lebedev, and M. E. Diamond, "The role of spike timing in the coding of stimulus location in rat somatosensory cortex," *Neuron* **29**, 769–777 (2001).
- ⁵⁸F. Montani, A. Kohn, M. A. Smith, and S. R. Schultz, "The role of correlations in direction and contrast coding in the primary visual cortex," *J. Neurosci.* **27**, 2338–2348 (2007).
- ⁵⁹M. A. Montemurro, S. Panzeri, M. Maravall, A. Alenda, M. R. Bale, M. Brambilla, and R. S. Petersen, "Role of precise spike timing in coding of dynamic vibrissa stimuli in somatosensory thalamus," *J. Neurophysiol.* **98**, 1871–1882 (2007).